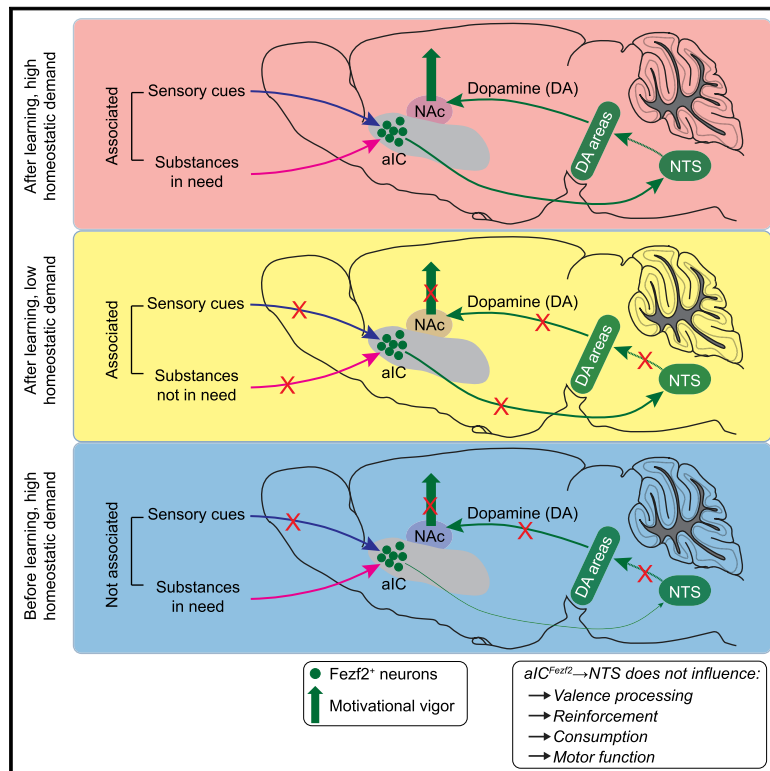# A genetically defined insula-brainstem circuit selectively controls motivational vigor

Graphical abstract

Authors

Hanfei Deng, Xiong Xiao, Tao Yang, ..., Yulong Li, Z. Josh Huang, Bo Li

Correspondence

deng@cshl.edu (H.D.),
bli@cshl.edu (B.L.)

In brief

An anterior insula-brainstem circuit is defined that specifically controls motivational vigor and dopamine release in a learning- and need-dependent manner, without influencing valence processing, reinforcement, consumption, and motor function.

Highlights

- Neurons in the aIC^{Fezf2} → NTS circuit acquire anticipatory activity through learning

- The anticipatory activity encodes the perceived value and motivation

- aIC^{Fezf2} → NTS controls vigor, effort, and striatal dopamine release

- aIC^{Fezf2} → NTS function depends on both learning and homeostatic demand

CellPress

Article

A genetically defined insula-brainstem circuit selectively controls motivational vigor

Hanfei Deng,[1,8,*] Xiong Xiao,[1,7,8] Tao Yang,[1] Kimberly Ritola,[2] Adam Hantman,[2] Yulong Li,[3,5,6] Z. Josh Huang,[4] and Bo Li[1,9,*]
[1]Cold Spring Harbor Laboratory, Cold Spring Harbor, NY 11724, USA
[2]HHMI Janelia Research Campus, Ashburn, VA 20147, USA
[3]State Key Laboratory of Membrane Biology, Peking University School of Life Sciences, Beijing 100871, China
[4]Department of Neurobiology, Duke University School of Medicine, Durham, NC 27710, USA
[5]PKU-IDG/McGovern Institute for Brain Research, Beijing 100871, China
[6]Peking-Tsinghua Center for Life Sciences, Beijing 100871, China
[7]Present address: Institute of Neuroscience, CAS Center for Excellence in Brain Science and Intelligence Technology, Chinese Academy of Sciences, Shanghai 200031, China
[8]These authors contributed equally
[9]Lead contact
*Correspondence: deng@cshl.edu (H.D.), bli@cshl.edu (B.L.)
https://doi.org/10.1016/j.cell.2021.11.019

SUMMARY

The anterior insular cortex (aIC) plays a critical role in cognitive and motivational control of behavior, but the underlying neural mechanism remains elusive. Here, we show that aIC neurons expressing *Fezf2* (aIC^{Fezf2}), which are the pyramidal tract neurons, signal motivational vigor and invigorate need-seeking behavior through projections to the brainstem nucleus tractus solitarii (NTS). aIC^{Fezf2} neurons and their postsynaptic NTS neurons acquire anticipatory activity through learning, which encodes the perceived value and the vigor of actions to pursue homeostatic needs. Correspondingly, aIC → NTS circuit activity controls vigor, effort, and striatal dopamine release but only if the action is learned and the outcome is needed. Notably, aIC^{Fezf2} neurons do not represent taste or valence. Moreover, aIC → NTS activity neither drives reinforcement nor influences total consumption. These results pinpoint specific functions of aIC → NTS circuit for selectively controlling motivational vigor and suggest that motivation is subserved, in part, by aIC's top-down regulation of dopamine signaling.

INTRODUCTION

An extensive body of literature from human studies indicates that the insular cortex (IC), especially the anterior IC (aIC), plays a pivotal role in integrating interoceptive and exteroceptive information into cognitive and motivational control of behavior (Craig, 2009; Critchley and Harrison, 2013; Menon and Uddin, 2010; Quadt et al., 2018). In particular, human neuroimaging studies show that the aIC is more activated during intrinsically motivating tasks than non-motivating ones (Lee and Reeve, 2013, 2017). Cues associated with drugs of abuse activate the IC in addicted individuals, with the activity positively correlated with self-reported craving (Bonson et al., 2002; Engelmann et al., 2012; Kühn and Gallinat, 2011; Luijten et al., 2011). In parallel, it has been reported that individuals with insular lesions have reduced energy or drive (Manes et al., 1999), or quit smoking easily without relapse (Naqvi et al., 2014; Naqvi et al., 2007). Furthermore, aIC dysfunction is associated with mood disorders including depression (Etkin, 2010; Collins et al., 2019; Paulus and Stein, 2010; Sliz and Hayley, 2012; Sprengelmeyer et al., 2011; Stratmann et al., 2014).

These studies strongly suggest a role of the aIC in motivation-related processes.

Studies in rodents have revealed detailed, yet divergent functions of the IC (Gogolla, 2017; Vincis and Fontanini, 2016). For example, IC neurons are involved in processing gustatory information (Chen et al., 2011, 2021; Katz et al., 2001; Samuelsen and Fontanini, 2017) and cue-reward association (Kusumoto-Yoshida et al., 2015; Livneh et al., 2017, 2020; Samuelsen et al., 2012). IC neurons are also involved in processing valence information, because activation of aIC neurons, for instance, produces positive valence and appetitive response (Peng et al., 2015; Wang et al., 2018). However, activation of aIC neurons can also produce negative valence and aversive response (Wu et al., 2020). Interestingly, inhibition of IC neurons (Contreras et al., 2007; Forget et al., 2010), or specific inhibition of aIC neurons (Venniro et al., 2017), reduces addictive behaviors, suggesting that the rodent IC is also critical for motivation, like its counterpart in humans. Nonetheless, given that learning, valence, and motivation are dissociable processes (Berke, 2018; Berridge et al., 2009; Mohebi et al., 2019; Shuvaev et al., 2021), it is unclear how the IC
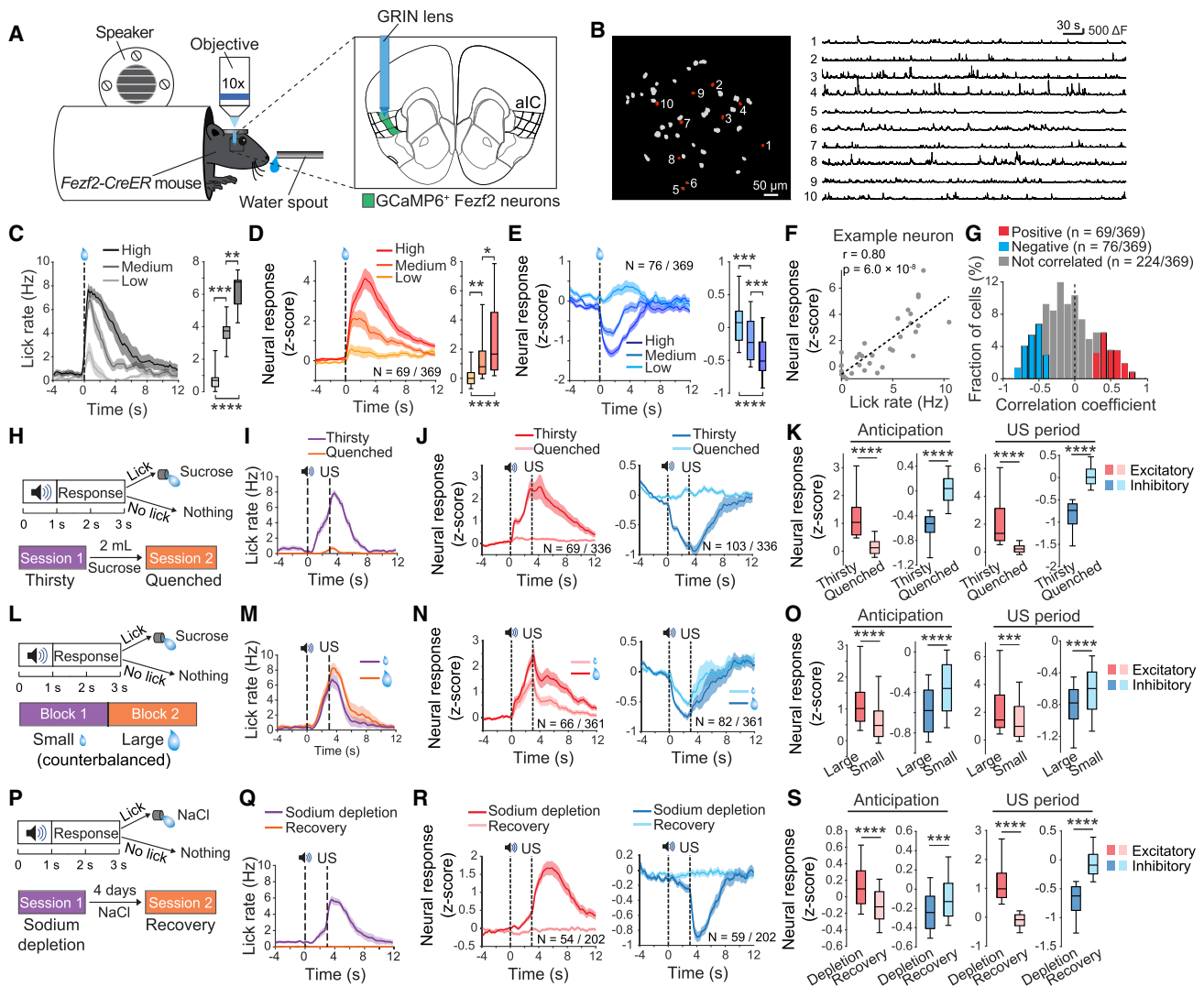
Figure 1. aIC^Fezf2 neuron activity is modulated by action vigor and motivational state

(A) Schematics of the setup (left) and location in the aIC (right) for imaging.

(B) Left: the spatial locations of individual extracted neurons. In red, 10 example neurons whose activity traces are shown in the right.

(C) Left: average licking rates in different trial types. Right: quantification of average licking rates during the 4-s period following tastant delivery ($F_{(2,15)} = 38.79$, $p < 0.0001$; **$p = 0.0022$, ***$p = 0.0009$, ****$p < 0.0001$; one-way ANOVA followed by Tukey's test).

(D) Left: average responses of the neurons showing significant positive correlations in (G) in different trial types. Right: quantification of average responses during the 4-s period following tastant delivery ($F_{(2,204)} = 17.32$, $p < 0.0001$; *$p = 0.014$, **$p = 0.0073$, ****$p < 0.0001$; one-way ANOVA followed by Tukey's test).

(E) Same as (D), except that the neurons are those showing significant negative correlations in (G) ($F_{(2,225)} = 32.35$, $p < 0.0001$; ***$p = 0.0001$ (low versus medium), ***$p = 0.0004$ (medium versus high), ****$p < 0.0001$; one-way ANOVA followed by Tukey's test).

(F) An example neuron showing a positive correlation between its responses and licking rates following US delivery (Pearson's $r = 0.80$, $p < 0.0001$). Each dot represents one trial.

(G) Distribution of all the neurons' Pearson's correlation coefficients calculated as in (F). Red, blue, and gray bars represent neurons showing significant positive ($p < 0.05$), significant negative ($p < 0.05$), and non-significant ($p > 0.05$) correlations, respectively.

(H) A schematic of the task.

(I) Average licking rates of a mouse in thirsty and quenched states.

(J) Average activity traces of neurons showing excitatory (left) or inhibitory (right) response under thirsty and quenched states.

(K) Quantification of the average responses shown in (J), during the anticipation (0–3 s; left) and US (3–5 s; right) periods (****$p < 0.0001$, Wilcoxon signed-rank test).

(L) A schematic of the task.

(M) Average licking rates of a mouse in the small- and large-reward blocks.

(N) Average activity traces of neurons showing excitatory (left) or inhibitory (right) response to the presentation of US in the large- and small-reward blocks.

(O) Quantification of the average responses shown in (N), during the anticipation (0–3 s; left) and US (3–5 s; right) periods (***$p < 0.001$, ****$p < 0.0001$, Wilcoxon signed-rank test).

(legend continued on next page)

orchestrates such divergent functions and how the IC controls motivation.

It is possible that the functional divergence is a manifestation of cell type heterogeneity. Indeed, studies on the IC have thus far targeted largely unspecified populations, which are highly heterogeneous (Dikecligil et al., 2020; Maffei et al., 2012). For projection neurons alone, there are hundreds of transcriptomic types (Tasic et al., 2018; Yao et al., 2021), with adjacent but transcriptionally distinct neurons having different connectivity (Chen et al., 2019; Matho et al., 2021; Zhang et al., 2021). Moreover, even neurons projecting to the same target can have opposing functions (Zhang et al., 2021). Therefore, neuronal type identity in combination with connectivity specificity may determine the functions of different insular populations.

In this study, we tested the hypothesis that aIC neurons projecting to the brainstem nucleus tractus solitarii (NTS) regulate motivational processes. The only cortical neurons that directly project to the brainstem are the large pyramidal tract (PT) neurons in layer 5B (Chen et al., 2019; Harris and Shepherd, 2015), which have distinct genetic identity, connectivity, and physiological properties compared with neighboring neurons (Harris and Mrsic-Flogel, 2013; Harris and Shepherd, 2015; Matho et al., 2021; Suter et al., 2013). Therefore, we used a genetic strategy combined with viral tools to target aIC PT neurons, as well as neurons along the aIC → NTS circuit. This approach allowed us to pinpoint highly specific functions of this circuit in motivational control.

RESULTS

The input and output connections of aIC^{Fezf2} neurons

Because PT neurons are specified by the master transcription factor forebrain expressed zinc finger 2 (Fezf2) (Harris and Shepherd, 2015; Lodato et al., 2014), we used a *Fezf2-CreER* knockin mouse driver—that expresses the inducible Cre recombinase (CreER) under the control of endogenous *Fezf2* promoter—to target PT neurons in the aIC. We injected the aIC of *Fezf2-CreER* mice with an adeno-associated virus (AAV) expressing GFP in a Cre-dependent manner (Figure S1A), followed by tamoxifen induction. We observed dense axon fibers originating from the labeled aIC PT neurons—hereafter referred to as aIC^{Fezf2} neurons—in brainstem areas (including the NTS and parabrachial nucleus [PBN]) and the thalamus (Figures S1B–S1F). There were also moderate to sparse fibers in forebrain areas, including the striatum, parasubthalamic nucleus, amygdala, and posterior IC (Figures S1G–S1K).

To examine the afferents of aIC^{Fezf2} neurons, we specifically infected these neurons with a rabies virus system (Figures S1L and S1M), which revealed that aIC^{Fezf2} neurons receive promi-

nent monosynaptic inputs from various sources, including the motor, somatosensory and prefrontal cortices, and insula itself (Figures S1N, S1O, and S1V); these neurons also receive strong inputs from the basolateral amygdala, thalamus, olfactory areas, hippocampal formation (Figures S1P–S1S and S1V), and midbrain and hindbrain areas, especially the dorsal raphe nucleus and PBN (Figures S1T–S1V).

aIC^{Fezf2} neurons represent motivational vigor

Next, we characterized the *in vivo* response properties of aIC^{Fezf2} neurons. We infected these neurons with the genetically encoded calcium indicator GCaMP6 (Chen et al., 2013) and implanted a gradient-index (GRIN) lens into the aIC (Figures 1A and S2A). This approach allowed imaging aIC^{Fezf2} neuron activities—represented as GCaMP6 signals—at cellular resolution through the GRIN lens in behaving mice (Figure 1B; Video S1).

We first examined how individual neurons responded to sweet and bitter tastes by providing the mice with sucrose and quinine solutions. Many neurons were excited, whereas others were inhibited during consumption of the two liquids (Figures S2B and S2C), with the excited and inhibited neurons intermingled with no obvious spatial clustering (Figures S2D and S2E). Notably, a large population was excited by both sucrose and quinine, whereas another population was inhibited by both tastants (Figures S2B, S2C, and S2F). Because the licking rate of mice exhibited apparent variability across trials (Figure 1C), a phenomenon known to reflect fluctuating motivation (Berditchevskaia et al., 2016), we examined if this variability was reflected in neural activity. Remarkably, the responses of a substantial fraction of neurons (~40% of 369 neurons imaged in 5 mice) scaled up or down with the licking rates during consumption (Figures 1D and 1E). Indeed, the neuronal response amplitudes showed either positive or negative trial-by-trial correlations with licking rates, regardless of whether the sucrose or quinine solution was consumed (Figures 1F, 1G, and S2G). In contrast, during baseline period (when liquid was unavailable), the activity of only few (~8.67%) of these neurons was correlated with mice's spontaneous licking (Figure S2H). These results suggest that a major population of aIC^{Fezf2} neurons represent the strength or vigor of licking, rather than taste or the movement associated with licking.

If aIC^{Fezf2} neurons represent action vigor, then their response should be dependent upon the animal's motivational state. To test this prediction, we trained these mice in a reward-seeking task, in which a sound (conditioned stimulus [CS]) predicted that a liquid reward (unconditioned stimulus [US]) would be delivered, but only if the mice licked the spout during a response window following the CS (Figures 1H, 1L, and 1P). We imaged the CS- and US-evoked responses of aIC^{Fezf2} neurons while the mice

---

(P) A schematic of the task.

(Q) Average licking rates of a mouse under sodium-depletion and after recovery.

(R) Average activity traces of neurons showing excitatory (left) or inhibitory (right) response to the presentation of US in mice under sodium depletion and after recovery.

(S) Quantification of the average responses shown in (R), during the anticipation (0–3 s; left) and US (3–5 s; right) periods (***p < 0.001, ****p < 0.0001, Wilcoxon signed-rank test).

Data are presented as mean ± SEM or box-and-whisker plots.
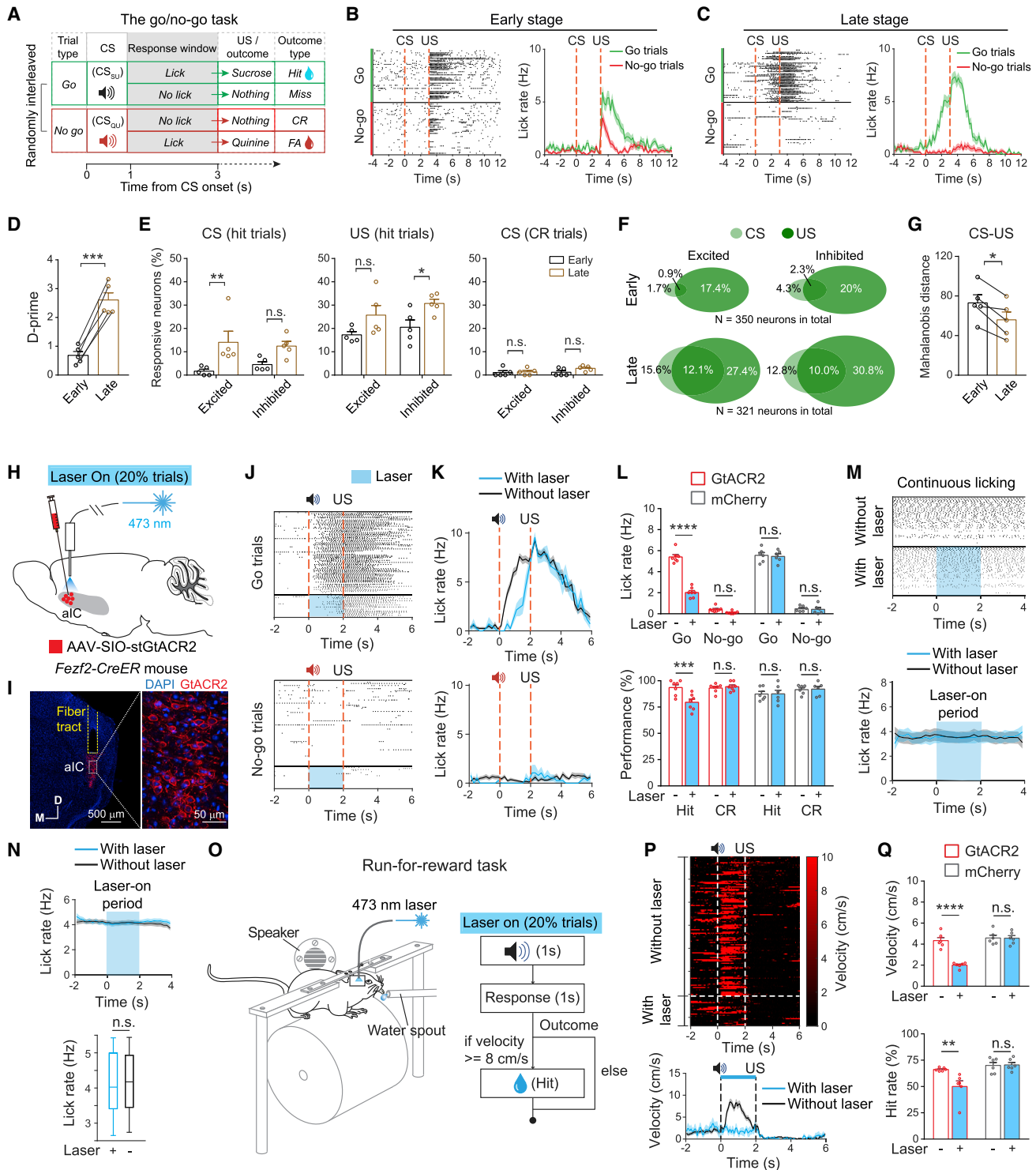
See also Figures S1, S2, and S3 and Video S1.

Figure 2. Learning induces anticipatory signals essential for motivational actions

(A) A schematic of the task design. CR, correct rejection; FA, false alarm.

(B and C) Licking events (left) and average licking rates (right) from a mouse at the early (B) and late (C) stages of training.

(D) D-prime at different stages of training ($t_{(4)}$ = 9.84, ***p = 0.0006, paired t test).

(E) Percentage of aIC^{Fezf2} neurons showing responses at different stages of training. Left: CS responses in hit trials ($F_{(1,16)}$ = 14.3, p = 0.0016; excited neurons, **p = 0.0098; inhibited neurons, p = 0.11). Middle: US responses in hit trials ($F_{(1,16)}$ = 10.85, p = 0.0046; excited neurons, p = 0.10; inhibited neurons, *p = 0.043).

(legend continued on next page)

transitioned between low and high levels of motivational drive under three distinct conditions. First, mice were kept thirsty and trained to lick for the delivery of a sucrose solution (Figure 1H). Well-trained thirsty mice showed increased anticipatory licking upon CS presentation; however, after free drinking was provided, the CS could no longer evoke licking, indicating that the mice were quenched (Figure 1I). We imaged aIC^Fezf2 neuron activity across thirsty and quenched states (Figures S2I and S2J). When the mice were thirsty, a substantial population of neurons responded to the CS, with one subset showing excitation and the other showing inhibition (Figures 1J, S2I, and S2J). Interestingly, both the excitatory and inhibitory responses followed characteristic ramping trajectories, starting from CS onset and reaching a peak or trough, respectively, upon US delivery (Figures 1J and S2J). However, such responses completely disappeared once the mice were quenched (Figures 1J, 1K, S2I, and S2J).

Second, the mice were kept thirsty and learned that the CS predicted a small drop (3 μL) of sucrose in one block, but the same CS predicted a large drop (12 μL) of sucrose in another block of trials (Figure 1L, M). We imaged the activity of aIC^Fezf2 neurons across the two blocks (Figures S2K–S2M), which presumably engaged with different levels of motivation. In both blocks, many neurons showed either excitatory or inhibitory response to the CS, but the response in the large-reward block was much larger than that in the small-reward block (Figures 1N, 1O, S2K, and S2L). However, the CS-evoked licking was comparable in the two blocks, although the US-evoked licking in the large-reward block was more vigorous (Figures 1M and S2M). These results suggest that aIC^Fezf2 neuron response reflects alterations in motivation levels preceding the occurrence of apparent motor changes.

Third, the mice were subject to a sodium-deficiency condition (Lee et al., 2019; Tindell et al., 2009) and learned that CS predicted the delivery of a high-sodium solution (500 mM NaCl) (Figure 1P), which is repellent to animals under normal conditions. The mice readily licked the spout following CS presentation (Figure 1Q), reflecting a homeostatic need for sodium. As expected,

the mice stopped responding to the CS after recovery from the deficiency (Figure 1Q). Remarkably, under sodium-deficiency, many aIC^Fezf2 neurons showed robust excitatory (27%) or inhibitory (29%) responses to sodium or the CS predicting sodium delivery, which were completely abolished after the mice had recovered from the deficiency (Figures 1R, 1S, S2N, and S2O).

To determine if the same neurons are involved in processing changing homeostatic demands, we tracked individual neurons across thirsty (Figure 1H) and sodium-deficiency (Figure 1P) states. Among the traceable neurons, a large fraction of those excited by sucrose solution when mice were thirsty (10 out of 18) were also excited by high-sodium when the mice were under sodium-deficiency (Figure S2P).

These results show that aIC^Fezf2 neuron response is potently modulated by action vigor, homeostatic demand, and the values of expected outcomes. In particular, these neurons represent the anticipation of outcomes that meet the changing needs of animals, even if the outcome—such as the high-sodium—is expected to be unpleasant. Thus, aIC^Fezf2 neurons integrate the learned, predictive signals with the information about homeostatic needs to represent anticipation and motivational vigor.

The anticipation response emerges during learning

To further investigate how aIC^Fezf2 neurons acquire anticipatory signals and participate in establishing motivated actions, we sought to image the activity of these neurons during learning in a "go/no-go" task (Figure 2A). In the "go" trials of this task, a sound (CS_SU) indicated that sucrose would be delivered, but only if mice licked the spout during a decision window ("hit"). In the "no-go" trials, another sound (CS_QU) announced that quinine would be delivered, but mice could avoid it by withholding licking in the decision window ("correct rejection" [CR]) (Figure 2A).

We imaged the activity of aIC^Fezf2 neurons at different stages of training (Figures 2B–2D and S2Q). By examining the activity of all the neurons in hit and CR trials, we found that initially very few neurons responded to CS; however, training dramatically increased the neurons showing excitatory response to

---

Right: CS responses in CR trials ($F_{(1,16)} = 1.05$, p = 0.32; excited neurons, n.s., p > 0.99; inhibited neurons, n.s., p = 0.21). Two-way ANOVA followed by Bonferroni's test.

(F) Percentage distributions of the neurons excited (left) and inhibited (right) by CS and US in hit trials at the early (top) and late (bottom) stages of training.

(G) Mahalanobis distance between vectors representing CS and US responses in hit trials at different stages of training ($t_{(4)} = 4.06$, *p = 0.015, paired t test).

(H) A schematic of the approach.

(I) Confocal images showing the expression of GtACR2 in aIC^Fezf2 neurons and optic fiber placement. On the right is a high-magnification image of the boxed area on the left.

(J and K) Licking rasters (J) and average licking rates (K) of a GtACR2 mouse in one session. Top: go trials. Bottom: no-go trials. Blue rectangles indicate the window of laser stimulation.

(L) Top: lick rate during anticipation period (0–2 s) (GtACR2: n = 7 mice, $F_{(1,12)} = 165.9$, p < 0.0001; go trials, ****p < 0 0.0001; no-go trials, n.s., p = 0.20; mCherry: n = 6 mice, $F_{(1,10)} = 0.011$, p = 0.92; go and no-go trials, n.s., p > 0.99). Bottom: performance (GtACR2: $F_{(1,12)} = 20.19$, p = 0.0007; hit, ***p = 0.0002; CR, n.s. (nonsignificant), p > 0.99; mCherry: $F_{(1,10)} = 0.012$, p = 0.92; hit and CR, p > 0.99). Two-way ANOVA followed by Bonferroni's test.

(M) Licking behavior of a GtACR2 mouse in the continuous licking task. Top: licking rasters. Bottom: average licking rates.

(N) Quantification of licking behavior in the continuous licking task. Top: average licking rate across mice. Bottom: average licking rate during the 0–2 s window (n = 7 mice; p = 0.59, Wilcoxon signed-rank test).

(O) Schematics of task setup (left) and design (right).

(P) Running behavior of a GtACR2 mouse in one session. Top: trial-by-trial velocity heatmap sorted according to trial types. Bottom: average running velocity; blue bar indicates the window of laser stimulation.

(Q) Top: running velocity during anticipation period (0–2 s) ($F_{(1,10)} = 59.95$, p < 0.0001; GtACR2, n = 6, ****p < 0.0001; mCherry, n = 6, n.s., p > 0.99). Bottom: hit rate ($F_{(1,10)} = 8.69$, p = 0.015; GtACR2, **p = 0.0048; mCherry, n.s., p > 0.99). Two-way ANOVA followed by Bonferroni's test.

Data are presented as mean ± SEM or box-and-whisker plots.

See also Figures S2, S3, and S4.

CS_{SU} and had a trend to increase the neurons showing inhibitory response to CS_{SU} (Figures 2E, 2F, S2R, and S2S). Training also increased sucrose-responsive neurons, especially those showing inhibitory response (Figures 2E and 2F). Very few neurons responded to CS_{QU} throughout training (Figure 2E).

Interestingly, training markedly increased the number of neurons responsive to both CS_{SU} and sucrose (excitation, p = 2.03×10^{-10}, inhibition, p = 2.62×10^{-5}, χ^2 test) (Figure 2F). Consistent with this observation, population analysis revealed that training led to an increase in similarity between the response to CS_{SU} and sucrose, quantified as a decrease in Mahalanobis distance between the ensemble representations of the two stimuli (Figure 2G). These results indicate that training fundamentally modifies the responsiveness of aIC^{Fezf2} neurons, such that the response to the reward cue becomes matched with that to the actual reward.

To further examine how the response of aIC^{Fezf2} neurons evolves during learning, we projected their population activity along the axes that optimally separated the anticipatory response in different trial types (Figure S2T). Robust predictive and ramping signals developed during training, such that the hit and CR trials became better separated at the late than early stage (Figure S2T). Consistently, training increased the difference between CS ensemble representations in hit and CR trials (Figures S2U and S2V). Furthermore, the CS population response can be used to decode go and no-go trials, with decoding accuracy dependent on learning (Figures S2W and S2X). These results suggest that learning induces robust anticipatory response in aIC^{Fezf2} population, which is specific for reward and can be used to instruct or invigorate reward-seeking behavior.

The anticipation response precedes actions and correlates with action strength

If aIC^{Fezf2} neurons act to invigorate behaviors, then their anticipatory activities are expected to occur earlier than, correlate with, and be required for motivated behaviors. To test these predictions, we first examined the relationship between neuronal and behavioral response in the reward-seeking task or the go/no-go task, during the time window when thirsty or sodium-depleted mice were anticipating sucrose or NaCl solution, respectively (Figures 1L, 1P, and 2A). Indeed, timing analysis revealed that most CS-excited neurons responded earlier than licking onset (Figures S3A, S3B, S3E, S3F, S3I, and S3J). Furthermore, trial-by-trial analysis showed that the response amplitudes of major aIC^{Fezf2} populations correlated with licking rates (Figures S3C, S3D, S3G, S3H, S3K, and S3L). These results are consistent with the notion that aIC^{Fezf2} neurons may provide signals that motivate or invigorate reward-seeking actions.

aIC^{Fezf2} anticipatory activity is required for motivational actions

Next, to determine the causal relationship between aIC^{Fezf2} neurons and motivational actions, we sought to specifically inhibit these neurons during anticipation with optogenetics (Figures 2H–2Q). For this purpose, we expressed a light-sensitive neuronal inhibitor GtACR2 (Govorunova et al., 2015; Mahn et al., 2018), or mCherry (as a control), selectively in aIC^{Fezf2} neu-

rons and implanted optical fibers above the infected areas for light delivery (Figures 2H and 2I). These mice were subsequently trained in the go/no-go task (Figure 2A). At the late stage of training, we delivered blue light into the aIC during the time window between CS onset and US onset, in randomly selected trials (Figures 2J–2L).

Strikingly, the photostimulation in the GtACR2 mice caused a dramatic reduction in anticipatory licking in go trials, resulting in decreased hit rate (Figures 2J–2L). These mice were not affected by the laser in no-go trials, but this was because licking was rare in these trials to begin with. As expected, the mCherry mice were not affected by the laser in either go or no-go trials (Figure 2L). Interestingly, once the GtACR2 mice had started licking in a "continuous licking" task, the photostimulation had no effect on the on-going licking behavior (Figures 2M and 2N). Thus, inhibiting aIC^{Fezf2} neurons impairs the anticipatory licking needed for obtaining reward, but does not affect the motor program underlying licking behavior.

To determine if aIC^{Fezf2} neurons are required specifically for licking, or generally for reward-seeking actions, we designed a "run-for-reward" (RFR) task in which mice needed to run upon CS presentation to obtain water reward (Stephenson-Jones et al., 2020) (Figure 2O). Once mice learned the task, we optogenetically inhibited aIC^{Fezf2} neurons during the window between CS onset and US onset in randomly selected trials (Figure 2O). This manipulation markedly reduced running velocity, leading to reduced performance in this task (Figures 2P and 2Q). Again, laser illumination in the aIC had no effect on the mCherry mice (Figure 2Q). Thus, aIC^{Fezf2} neurons are essential for promoting running to obtain reward.

We also examined whether inhibiting aIC^{Fezf2} neurons could influence valence processing, general body movements, or consumption. We found that, in a real-time place preference or aversion (RTPP/A) test, inhibition of aIC^{Fezf2} neurons did not cause preference or aversion; neither did it affect animals' movement (Figures S4A–S4E). In addition, inhibiting aIC^{Fezf2} neurons did not affect *ad libitum* sucrose consumption (Figures S4F and S4G).

Together, these results indicate that aIC^{Fezf2} neuron activity is required for the volitional aspect of reward-seeking actions but is dispensable for motor functions or consumption.

$aIC^{Fezf2} \rightarrow$ NTS activation invigorates motivational licking

aIC^{Fezf2} neurons send dense projections to the NTS (Figures S1A and S1B), consistent with previous observations that the IC sends long-range direct projections to the NTS (Jin et al., 2021; Shipley, 1982). Therefore, we tested if the functions of aIC^{Fezf2} neurons we observed are conveyed through $aIC^{Fezf2} \rightarrow$ NTS pathway. We first examined the composition of aIC projections to the NTS. More than 90% of NTS-projecting aIC neurons were *Fezf2*-expressing (*Fezf2*$^+$) (Figures 3A–3D), demonstrating that aIC $\rightarrow$ NTS projections originate predominately from aIC^{Fezf2} neurons.

We then probed $aIC^{Fezf2} \rightarrow$ NTS function with optogenetics. To this end, we bilaterally infected aIC^{Fezf2} neurons with an AAV expressing the light-gated cation channel ChR2, or GFP, and implanted optical fibers in the NTS above the axons
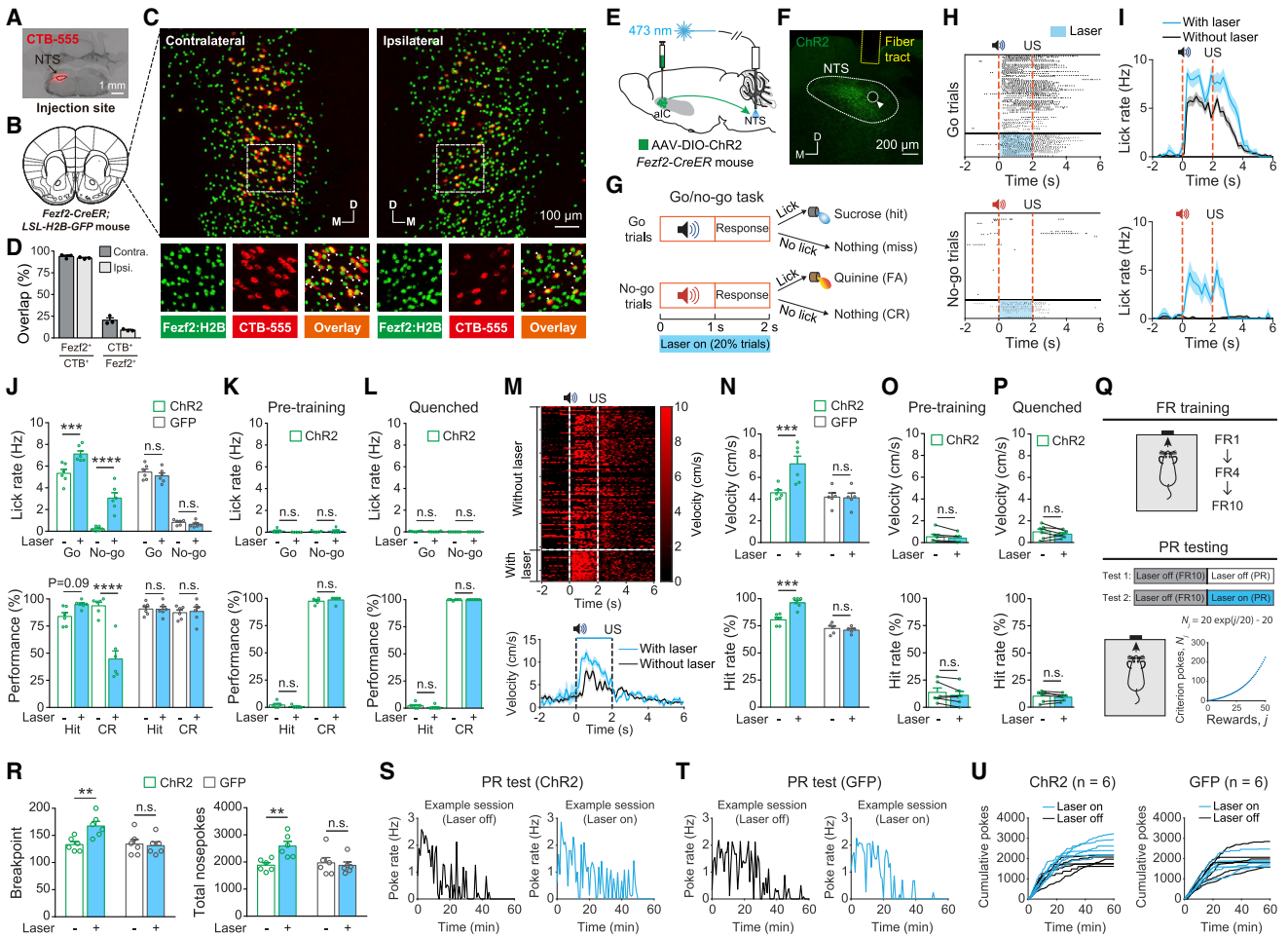
Figure 3. aIC^Fezf2→NTS activation promotes motivational vigor and effort

(A) An image showing CTB-555 injection in the NTS in a *Fezf2-CreER;LSL-H2B-GFP* mouse.

(B) A schematic of the brain section containing the aIC.

(C) Top: confocal images of retrogradely labeled aIC^NTS neurons (red) and Fezf2+ neurons (green) in the contralateral (left) and ipsilateral (right) aIC relative to the injection site in the NTS. Bottom: images of the boxed areas in the top panel. White arrowheads indicate double labeled neurons (yellow). D, dorsal; M, medial.

(D) Left two bars, percentages of co-labeled neurons (yellow) in all the retrogradely labeled neurons (red) in the contralateral (93.91% ± 1.37%) and ipsilateral (92.08% ± 0.63%) aIC (n = 3 mice). Right two bars, percentages of CTB+ neurons (red) in the Fezf2+ neurons (green) in the contralateral (20.36% ± 2.72%) and ipsilateral (9.01% ± 0.68%) aIC (n = 3 mice).

(E) A schematic of the approach.

(F) A confocal image showing optic fiber placement and axon fibers in the NTS, which originated from aIC^Fezf2 neurons. White arrowhead indicates the solitary tract.

(G) A schematic of the experimental design.

(H and I) Licking rasters (H) and average licking rates (I) of a ChR2 mouse in one session. Top: go trials. Bottom: no-go trials. Blue rectangles indicate the window of laser stimulation.

(J) Top: lick rate during anticipation period (0–2 s) (ChR2: n = 6 mice, $F_{(1,10)}$ = 86.58, p < 0.0001; go trials, ***p = 0.001; no-go trials, ****p < 0.0001; GFP: n = 6 mice, $F_{(1,10)}$ = 0.59, p = 0.46; go trials, p = 0.061; no-go trials, p = 0.37). Bottom: performance (ChR2: $F_{(1,10)}$ = 76.68, p < 0.0001; hit, p = 0.091; CR, ****p < 0.0001; GFP: $F_{(1,10)}$ = 0.11, p = 0.75; hit, p > 0.99; CR, p > 0.99). Two-way ANOVA followed by Bonferroni's test.

(K) Behavior of the ChR2 mice (n = 5) at the pre-training stage. Top: licking rates during anticipation period (0–2 s) ($F_{(1,8)}$ = 1.03, p = 0.34; go trials, p = 0.63; no-go trials, p > 0.99). Bottom: performance ($F_{(1,8)}$ = 1.77, p = 0.22; hit, p = 0.59; CR, p = 0.93). Two-way ANOVA followed by Bonferroni's test.

(L) Behavior of quenched ChR2 mice (n = 6) at the late training stage. Top: licking rates during anticipation period (0-2 s) ($F_{(1,10)}$ = 0.40, p = 0.54; go trials, p = 0.50; no-go trials, p > 0.99). Bottom: performance ($F_{(1,10)}$ = 1.26, p = 0.29; hit, p = 0.40; CR, p > 0.99). Two-way ANOVA followed by Bonferroni's test.

(M) Running behavior of a ChR2 mouse in one session. Top: trial-by-trial velocity heatmap. Bottom: average running velocity; blue bar indicates the window of laser stimulation.

(N) Top: running velocity during anticipation period (0–2 s) ($F_{(1,9)}$ = 21.47, p = 0.0012; ChR2, n = 6, ***p = 0.0002; GFP, n = 5, p > 0.99). Bottom: hit rate ($F_{(1,9)}$ = 18.91, p = 0.0019; ChR2, ***p = 0.0005; GFP, p > 0.99). Two-way ANOVA followed by Bonferroni's test.

(O) Behavior of the ChR2 mice (n = 6) at the pre-training stage. Top: running velocity during anticipation period (0–2 s) ($t_{(5)}$ = 1.50, p = 0.19, paired t test). Bottom: hit rate ($t_{(5)}$ = 1.92, p = 0.11, paired t test).

originating from the infected neurons (Figures 3E and 3F). These mice underwent training in the go/no-go task (Figure 3G). At the late stage of training, we delivered blue light pulses into the NTS during the window between CS onset and US onset in randomly selected trials (Figures 3E–3H).

Remarkably, the photostimulation in the ChR2 mice caused an increase in licking rate following CS presentation in not only go trials, but also no-go trials (Figures 3H and 3I). As a result, the CR rate was reduced; the hit rate was increased, although without reaching significance due to a ceiling effect (p = 0.09) (Figure 3J). Interestingly, before training in the task, the photostimulation did not induce any licking following either the go or the no-go tone, even though the mice were thirsty (Figure 3K). Moreover, after these mice were well trained but quenched, the photostimulation also failed to promote licking in the task (Figure 3L). The GFP mice were not affected by the laser (Figure 3J). These results suggest that $aIC^{Fezf2} \to NTS$ activity invigorates the learned, anticipatory licking response to obtain a homeostatic need; however, it does not override satiety signals or autonomously activate the motor program to generate licking.

$aIC^{Fezf2} \to NTS$ promotes vigor and effort

To determine if $aIC^{Fezf2} \to NTS$ is only involved in licking, we trained mice to perform the RFR task described above (Figure 2O), and optogenetically activated their $aIC^{Fezf2} \to NTS$ during the anticipation window (Figures 3M–3P). This manipulation markedly increased the velocity of anticipatory running and led to improved performance (Figures 3M and 3N). However, the same manipulation did not promote running before these mice were trained in the task (Figure 3O); it also failed to promote anticipatory running after the same mice were fully trained but quenched (Figure 3P). Laser illumination in the NTS had no effect on the GFP mice (Figure 3N). Thus, the results in the RFR and go/no-go tasks together demonstrate that $aIC^{Fezf2} \to NTS$ activity is capable of promoting different forms of volitional actions, on the condition that such actions have been learned and the outcome is homeostatically needed. In other words, $aIC^{Fezf2} \to NTS$ activity invigorates "need seeking," but does not override homeostasis or automatically lead to action generation.

Next, we tested mice in a progressive-ratio (PR) task (Figures 3Q–3U). In this task, the effort required for thirsty mice to attain water increased progressively, and the breakpoint at which the mice stopped responding was used as a measure of motivation (Figure 3Q). In some sessions, we optogenetically activated $aIC^{Fezf2} \to NTS$. This manipulation significantly increased the breakpoint and the total number of reward-seeking actions (Figures 3R–3U). Thus, $aIC^{Fezf2} \to NTS$ activation promotes the effort an animal spends in pursuing reward.

Notably, we found that optogenetically activating this pathway did not induce appetitive (or aversive) responses, neither did it affect animals' locomotion in the RTPP/A test (Figures S4H–S4L). Activating this pathway also failed to support self-stimulation (Figures S4M–S4O). To test whether $aIC^{Fezf2} \to NTS$ activation promotes consumption, we activated the $aIC^{Fezf2} \to NTS$ pathway in hungry or thirsty mice in the presence of food or water, respectively. The activation did not increase food or water intake (Figures S4P and S4Q). In a separate test, activating this pathway also did not affect *ad libitum* sucrose consumption (Figures S4F and S4R). These results show that $aIC^{Fezf2} \to NTS$ activity does not produce valence, affect movement, or influence food and liquid consumption.

Together, these results strongly suggest that $aIC^{Fezf2} \to NTS$ carries out the invigoration function of aIC^{Fezf2} neurons and promotes the effort of motivational actions.

The dependence on the perceived value

Next, we systematically examined the effects of $aIC^{Fezf2} \to NTS$ activation in well-trained mice performing the reward-seeking task (Figures 4A–4G). We found that in a quenched state, activating $aIC^{Fezf2} \to NTS$ did not induce anticipatory licking that would lead to water delivery (Figures 4A–4C, 4F, and 4G, leftmost). In contrast, in a thirsty state, activating this pathway dramatically increased the rate of anticipatory licking for either water or a sucrose solution, and even for a NaCl solution (300 mM), albeit to a lower level (Figures 4D and 4F). As a result, the performance in these sessions was improved (Figure 4G). The activation also potently promoted anticipatory licking for Ensure (a liquid food) when the mice were hungry (Figures 4E–4G, rightmost). However, the activation failed to increase anticipatory licking in sessions in which quinine was the US, or when no US was delivered (i.e., in extinction), even if the mice were thirsty (Figures 4D, 4F, and 4G). These results thus confirm that $aIC^{Fezf2} \to NTS$ function depends on homeostatic needs and further suggest that it depends on the perceived values of outcomes under on-going homeostatic demands.

The aIC^{NTS} subpopulation is enriched with anticipation signals

To monitor the endogenous function of $aIC^{Fezf2} \to NTS$ pathway, we selectively imaged the activity of the NTS-projecting subpopulation of aIC^{Fezf2} neurons. Because essentially all NTS-projecting neurons in the aIC (aIC^{NTS}) are $Fezf2^+$ (Figures 3A–3D), we labeled aIC^{NTS} neurons with GCaMP6 for the imaging, by injecting the NTS of wild-type mice with a retrograde AAV expressing Cre, and injecting the aIC of the same animals with the AAV expressing GCaMP6 Cre-dependently (Figure 5A). We imaged the

---

(P) Behavior of quenched ChR2 mice (n = 6) after training. Top: running velocity during anticipation period (0–2 s) ($t_{(5)}$ = 1.18, p = 0.29, paired t test). Bottom: hit rate ($t_{(5)}$ = 1.23, p = 0.27, paired t test).

(Q) Schematics of the task design for fixed-ratio (FR) and progressive-ratio (PR).

(R) Left: breakpoint: $F_{(1,10)}$ = 11.07, p = 0.0077; ChR2, n = 6, **p = 0.0029; GFP, n = 6, n.s., p > 0.99. Right: total nose pokes: $F_{(1,10)}$ = 16.17, p = 0.0024; ChR2, **p = 0.0011; GFP, n.s., p > 0.99. Two-way ANOVA followed by Bonferroni's test.

(S and T) Nose poke rate during PR test for a ChR2 (S) and GFP (T) mouse.

(U) Cumulative nose pokes for the ChR2 (left) and GFP (right) mice during PR test.
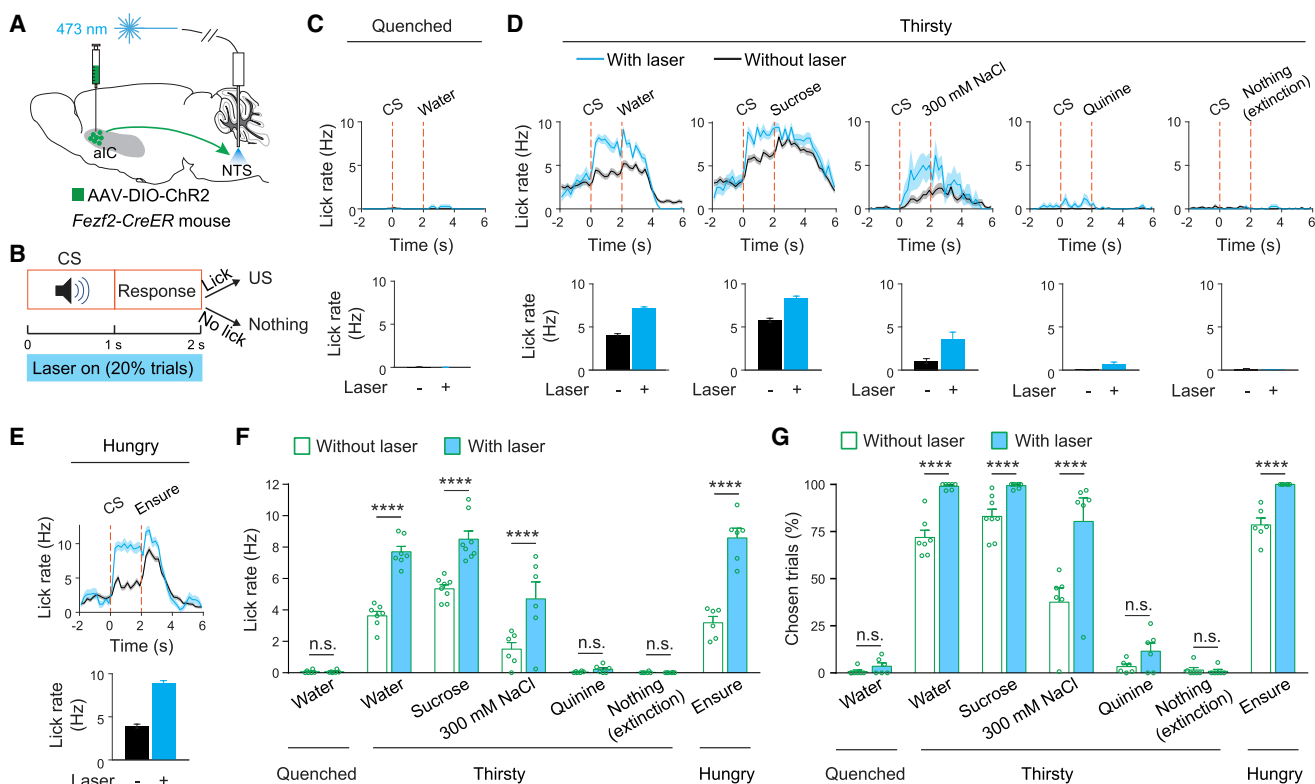
Data are presented as mean ± SEM.

See also Figure S4.

Figure 4. aIC^Fezf2 → NTS function depends on the perceived values

(A and B) Schematics of the approach (A) and experimental design (B).

(C–E) Average licking rate traces (top) and licking rate during anticipation period (bottom) in representative sessions of differing conditions. (C) Quenched condition. (D) Thirsty condition. (E) Hungry condition.

(F) Licking rate during anticipation period in the ChR2 mice under differing conditions ($F_{(6,38)}$ = 23.96, p < 0.0001; quenched: water, n.s., p > 0.99; thirsty: water, sucrose and NaCl, ****p < 0.0001; thirsty: quinine and extinction, n.s., p > 0.99; hungry: ensure, ****p < 0.0001; two-way ANOVA followed by Bonferroni's test).

(G) Performance, quantified as the fraction of trials the mice licked during the anticipation period, in the ChR2 mice under differing conditions ($F_{(6,38)}$ = 16.45, p < 0.0001; quenched: water, n.s., p > 0.99; thirsty: water, sucrose and NaCl, ****p < 0.0001; thirsty: quinine, n.s., p = 0.24; extinction, n.s., p > 0.99; hungry: ensure, ****p < 0.0001; two-way ANOVA followed by Bonferroni's test).

Data are presented as mean ± SEM.

activity of aIC^NTS neurons as we did for aIC^Fezf2 neurons (Figures 5A and 5B).

Like aIC^Fezf2 neurons, aIC^NTS neurons showed excitatory or inhibitory response to sucrose and quinine that scaled up or down with the licking rates of the mice (Figures S5A–S5C). Moreover, the response amplitudes of many neurons showed positive or negative correlations with the licking rates during liquid consumption (Figures S5D and S5E) but not during baseline periods (Figure S5F). Interestingly, compared with aIC^Fezf2 neurons, a much larger fraction of aIC^NTS neurons showed excitatory response to sucrose (aIC^NTS, 34.5%; aIC^Fezf2, 19.5%) or to both sucrose and quinine (aIC^NTS, 14%; aIC^Fezf2, 8.4%) (Figures S5G and S5H).

In the reward-seeking task in which the size of reward was variable, the anticipatory response—either excitatory or inhibitory—of many aIC^NTS neurons in big-reward trials was larger than that in small-reward trials (Figures 5C–5G). Furthermore, the anticipatory neuronal response preceded and correlated with mice's licking action (Figures 5H–5K). Notably, compared with aIC^Fezf2 neurons imaged in the same task (Figure S3D), a much greater

fraction of aIC^NTS neurons showed such correlative responses (aIC^NTS, 79.2%; aIC^Fezf2, 36%) (Figure 5L). In addition, although the anticipatory response of either aIC^Fezf2 or aIC^NTS could be used to classify between small- and big-reward trials, aIC^NTS was better in decoding performance (Figure 5M). These results together indicate that the aIC^NTS subpopulation is more enriched with the anticipation or vigor signals than the larger aIC^Fezf2 population and thus may convey these signals to the NTS.

Anticipation signals emerge in NTS^Recipient neurons during learning

To determine whether the anticipation signals in aIC^Fezf2 or aIC^NTS neurons are conveyed to the NTS, we monitored the activity of the NTS neurons receiving direct synaptic inputs from the aIC—termed NTS^Recipient neurons. To target NTS^Recipient neurons, we bilaterally injected the aIC of wild-type mice with an anterograde transsynaptic AAV1-Cre (Zingg et al., 2017) and injected the NTS of the same animals with the Cre-dependent GCaMP6 AAV (Figures S5I and S5J). Optical fibers were
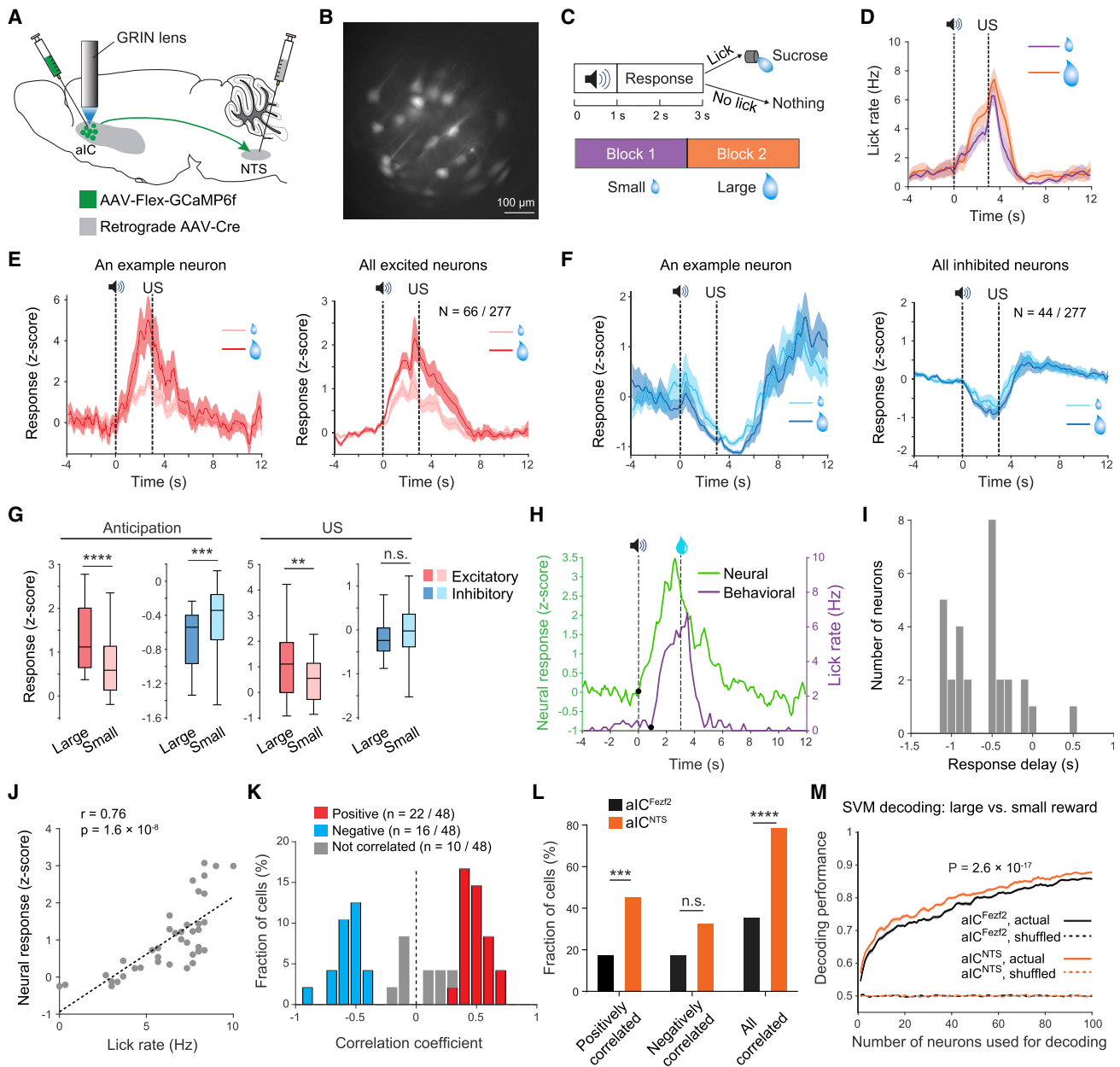
Figure 5. aIC^NTS neurons are enriched with the anticipatory vigor signals

(A) A schematic of the approach.

(B) A field of view showing the raw GCaMP6f fluorescence signals in aIC^NTS neurons.

(C) A schematic of the task design.

(D) Average licking rates in the small-reward and large-reward blocks.

(E) Activity traces of aIC^NTS neurons showing excitatory responses to US. Left: an example neuron. Right: all neurons.

(F) Same as (E) except that data are from aIC^NTS neurons with inhibitory responses.

(G) Quantification of the average responses shown in (E) and (F), during the anticipation (0–3 s; left) and US (3–5 s; right) periods (**p < 0.01; ***p < 0.001; ****p < 0.0001; n.s., p > 0.05; Wilcoxon signed-rank test).

(H) The timing of CS-induced excitation and licking in an aIC^NTS neuron and the corresponding mouse, respectively. Black dots represent change points.

(I) The difference between neural and behavioral change-points for all the CS-excited neurons.

(J) A neuron showing a positive correlation between its responses and licking rates in the 3-s time window immediately after CS onset (Pearson's r = 0.76, p < 0.0001). Each dot represents one trial.

(K) Distribution of all the CS-responsive neurons' Pearson's correlation coefficients calculated as in (J). Red, blue and gray bars represent neurons showing significant positive (p < 0.05), significant negative (p < 0.05) and nonsignificant (p > 0.05) correlations, respectively.

(L) The fraction of aIC^Fezf2 and aIC^NTS neurons showing the significant correlations (positive, ***p = 0.00065; negative, n.s., p = 0.059; all, ****p < 0.0001; χ² test).

(legend continued on next page)

subsequently implanted into the NTS, above the infected NTS[Recipient] neurons (Figures S5I and S5J).

We recorded the bulk activities of NTS[Recipient] neurons in these mice with fiber photometry, at different stages of training in the go/no-go task (Figures S5K–S5M). At the early stage of training, NTS[Recipient] neurons showed little response following CS presentations in either the go or no-go trials (Figures S5N, S5O, and S5R). However, at the late stage, these neurons displayed ramping-up activities following CS presentations until sucrose was delivered in the go trials (Figures S5P–S5S). In contrast, such anticipatory response was absent in the no-go trials. Thus, the anticipation response of NTS[Recipient] neurons, which bears characteristics of that of aIC[Fezf2] neurons, emerges during learning, paralleling the establishment of need-seeking behavior.

NTS[Recipient] activity is required for need-seeking actions

To determine if the anticipatory activity of NTS[Recipient] neurons is required for need-seeking behavior, we specifically inhibited these neurons during anticipation in mice performing the go/no-go task (Figures 6A–6E). Strikingly, this manipulation caused a dramatic decrease in the anticipatory licking in go trials, resulting in impaired performance (Figures 6C–6E). In contrast, the inhibition had no effect on the on-going licking behavior in the continuous licking task (Figures 6F and 6G).

Furthermore, in the RFR task, inhibition of NTS[Recipient] neurons during anticipation markedly reduced the anticipatory running and performance (Figures 6H and 6I). However, inhibiting these neurons did not induce aversion or preference or any change in movement in the RTPP/A test (Figures S4S–S4W); it also did not affect ad libitum sucrose consumption (Figures S4F and S4X). Together, these results demonstrate that NTS[Recipient] activity is essential for the anticipatory control of different forms of goal-directed actions but dispensable for motor function or consumption.

aIC[Fezf2] → NTS promotes dopamine release when the outcome is needed

To map the downstream targets that may mediate the function of NTS[Recipient] neurons, we labeled these neurons with GFP (Figures S6A and S6B). Notably, we found dense GFP-labeled axon fibers in dopamine areas including the retrorubral field (RRF)—that is populated by the A8 dopaminergic neuron group (Figure S6C) (Fu et al., 2012)—and the visual tegmental relay zone (VTRZ), a brain region located next to the ventral tegmental area (VTA) (Figure S6D). In both areas, the axon fibers were in close proximity to dopamine neurons (Figures S6C and S6D). Axon fibers were also observed in the thalamus (Figure S6E) and PBN (Figure S6F). Thus, NTS[Recipient] neurons can potentially influence dopamine neuron function through their direct projections to the RRF or VTRZ or through an indirect pathway via the PBN (Figure S6G).

Dopamine signaling in the nucleus accumbens (NAc) is involved in the modulation of action vigor (Floresco, 2015; du Hoffmann and Nicola, 2014; Hamid et al., 2016; Ko and Wanat, 2016; Mohebi et al., 2019). Therefore, we examined whether aIC[Fezf2] → NTS can regulate NAc dopamine release. We bilaterally expressed ChR2 in aIC[Fezf2] neurons and also expressed a genetically encoded dopamine sensor DA2m (Sun et al., 2018, 2020) in NAc neurons of the same mice. Optical fibers were subsequently implanted in the NTS and NAc for photostimulation and fiber photometry, respectively (Figures 7A and 7B).

We trained these mice to perform the go/no-go task while recording dopamine release in the NAc with photometry. In randomly selected trials, we moderately photostimulated aIC[Fezf2] → NTS during the anticipation period (Figures 7C and 7D). In the absence of the stimulation ("no laser"), dopamine release increased and decreased following CS in go and no-go trials, respectively (Figures 7E–7I). Interestingly, the stimulation ("laser") further enhanced the increase in dopamine release in go trials, and prevented the decrease in dopamine release in no-go trials (Figures 7E, 7G, and 7I).

The observed enhancement of dopamine release was unlikely secondary to an increase in licking, because activating aIC[Fezf2] → NTS did not affect licking in no-go trials, but still enhanced dopamine release (Figure 7H and 7I). Furthermore, we selected "no-laser" and "laser" go trials with similar anticipatory licking rates (Figure 7J; STAR Methods). Analysis on such licking rate-matched go trials still showed that aIC[Fezf2] → NTS activation was accompanied by an increase in dopamine release (Figures 7K and 7L). In the GFP control mice, shining light in the NTS had no effect (Figures 7M and 7N).

Finally, we repeated the activation when the mice were quenched, which failed to affect dopamine release in either go or no-go trials (Figures 7O–7Q). These results together indicate that aIC[Fezf2] → NTS promotes dopamine release in the NAc but only when the outcome is homeostatically needed.

DISCUSSION

Features of the aIC[Fezf2] → NTS circuit

The aIC[Fezf2] → NTS circuit exhibited several distinctive features. First, aIC[Fezf2] → NTS function strictly depended upon homeostatic needs. This circuit does not mediate the conventional reward-seeking function, which typically drives positive reinforcement and overconsumption (Berridge et al., 2009). Rather, it carries out a "need-seeking" function that is engaged only when a goal is homeostatically needed. Second, the response of a large fraction of aIC[Fezf2] or aIC[NTS] neurons did not represent sweet or bitter taste. Third, aIC[Fezf2] → NTS only invigorated learned actions, but did not influence movement per se. Fourth, a stable set of aIC[Fezf2] neurons participated in processing changing homeostatic needs. Our results altogether suggest that the aIC[Fezf2] → NTS circuit constitutes a common neural substrate that integrates learned, predictive signals with the information about fluctuating homeostatic needs to encode and regulate the motivational vigor of need-seeking behaviors.

(M) The performance of aIC[Fezf2] and aIC[NTS] neural activities during CS period in decoding large- versus small-reward trials (****p < 0.0001, Wilcoxon signed-rank test). Actual or shuffle: decoding analysis using actual neuron activities in large- and small-reward trials, or neuron activities shuffled across trial types.
Data are presented as mean ± SEM or box-and-whisker plots.
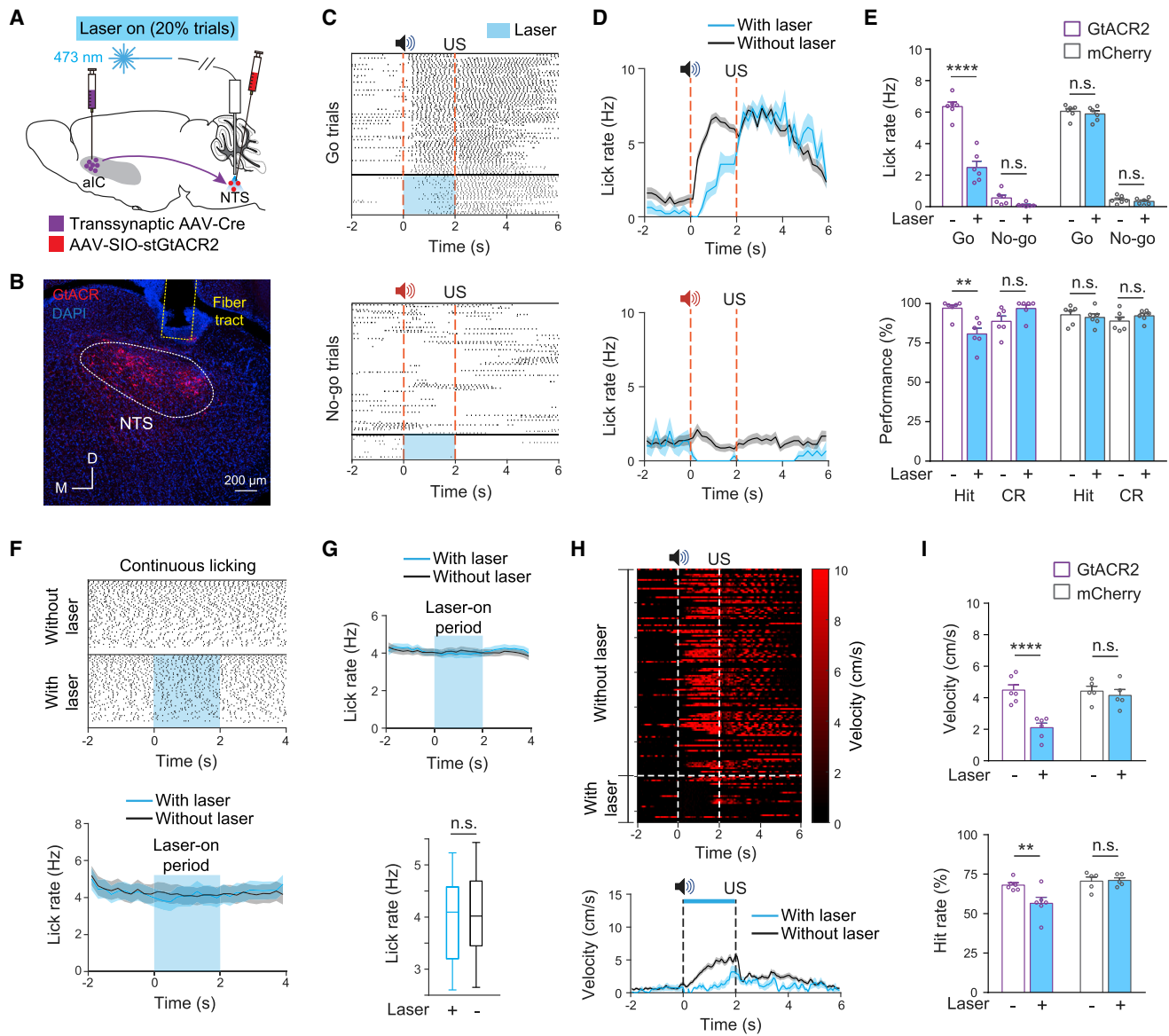See also Figure S5.

Figure 6. Inhibiting NTS^Recipient neurons during anticipation impairs motivational actions

(A) A schematic of the approach.

(B) A confocal image showing the expression of GtACR2 in NTS^Recipient neurons and the placement of optical fiber.

(C and D) Licking rasters (C) and average licking rates (D) of a GtACR2 mouse in one session. Top: go trials. Bottom: no-go trials. Blue rectangles indicate the window of laser stimulation.

(E) Top: lick rate during anticipation period (0–2 s) (GtACR: n = 6 mice, $F_{(1,10)}$ = 56.55, p < 0.0001; go trials, ****p < 0.0001; no-go trials, n.s., p = 0.38; mCherry: n = 6 mice, $F_{(1,10)}$ = 0.15, p = 0.71; go trials, n.s., p = 0.27; no-go trials, n.s., p = 0.62). Bottom: performance (GtACR: $F_{(1,10)}$ = 16.11, p = 0.0025; hit, **p = 0.0073; CR, n.s., p = 0.17; mCherry: $F_{(1,10)}$ = 3.74, p = 0.082; hit, n.s., p = 0.79; CR, n.s., p = 0.19). Two-way ANOVA followed by Bonferroni's test.

(F) Licking behavior of a GtACR2 mouse in the continuous licking task. Top: licking rasters. Bottom: average licking rates.

(G) Top: average licking rate across mice. Bottom: average licking rate during the 0–2 s window (n = 6 mice; p = 0.30, Wilcoxon signed-rank test).

(H) Running behavior of a GtACR2 mouse in one session. Top: trial-by-trial velocity heatmap. Bottom: average running velocity; blue bar indicates the window of laser stimulation.

(I) Top: running velocity during anticipation period (0–2 s) ($F_{(1,9)}$ = 22.69, p = 0.001; GtACR2, n = 6, ****p < 0.0001; mCherry, n = 5, n.s., p = 0.86). Bottom: hit rate ($F_{(1,9)}$ = 12.12, p = 0.0069; GtACR2, **p = 0.0016; mCherry, n.s., p > 0.99). Two-way ANOVA followed by Bonferroni's test.

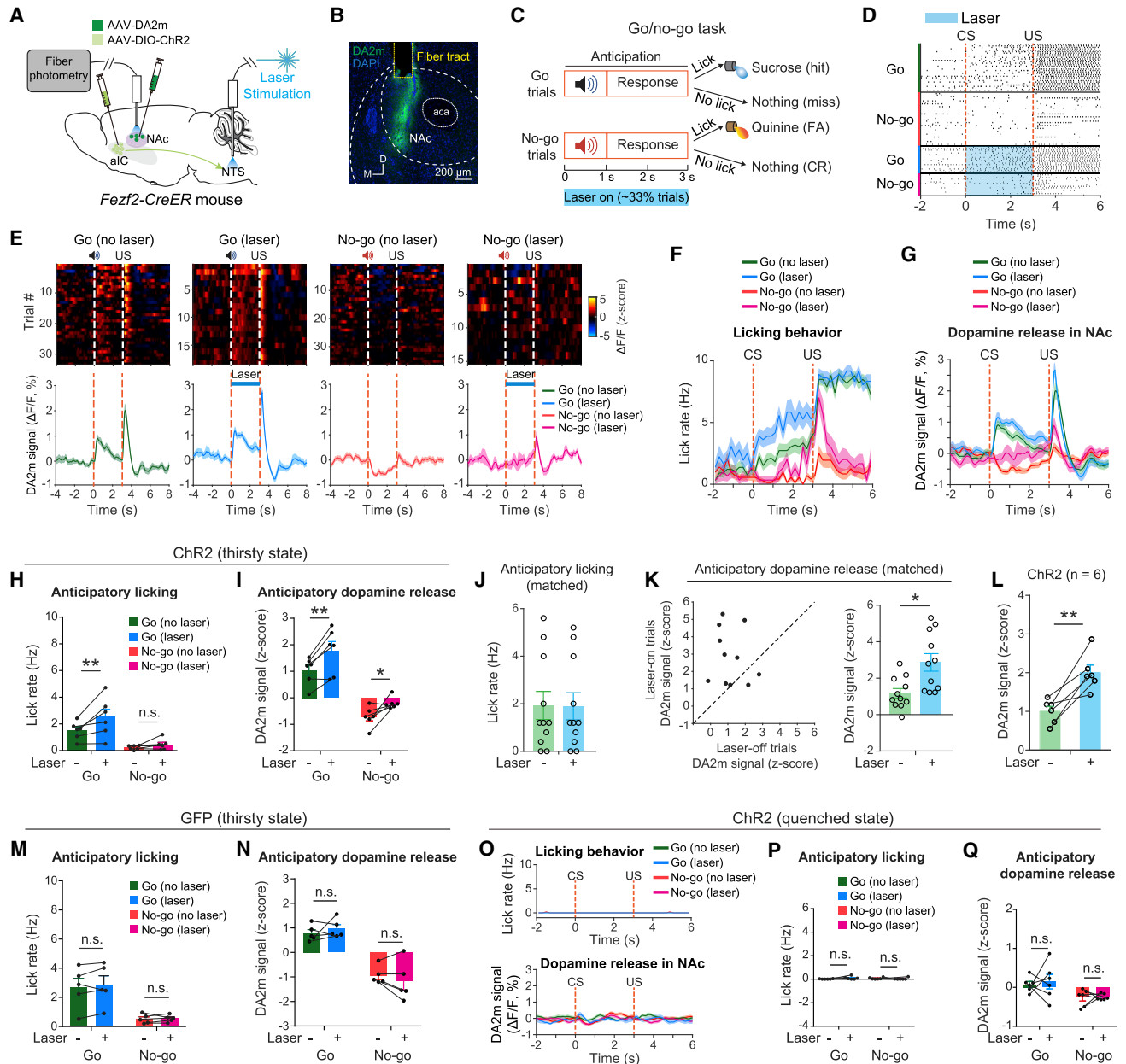Data are presented as mean ± SEM or box-and-whisker plots.

See also Figure S4.

Figure 7. aIC^Fezf2 → NTS activity promotes NAc dopamine release in a need-dependent manner

(A) A schematic of the approach.

(B) A confocal image showing the expression of DA2m in NAc core and the placement of optical fiber for photometry. Aca, anterior commissure.

(C) A schematic of task structure.

(D–N) Results obtained in thirsty state.

(D) Licking rasters of a ChR2 mouse in one session. Blue rectangles indicate the window of laser stimulation.

(E) Trial-by-trial (top) and average (bottom) dopaminergic activity in the NAc from the same session as that in (D). Blue bars indicate the window of laser stimulation.

(F and G) Average licking rates (F) and DA2m signals in the NAc (G) from the same mouse as in (D).

(H) Licking rate of all ChR2 mice during anticipation period (0–3 s) in different trial types ($F_{(1,10)}$ = 9.645, p = 0.011; go trials, **p = 0.0096; no-go trials, n.s., p = 0.70). Two-way ANOVA followed by Bonferroni's test.

(I) DA2m signals in the NAc of all the ChR2 mice during anticipation period (0-3 s) in different trial types ($F_{(1,10)}$ = 25.94, p = 0.0005; go trials, **p = 0.0034; no-go trials, *p = 0.028). Two-way ANOVA followed by Bonferroni's test.

(J) Licking rate data from a ChR2 mouse in selected go-trials in one session, in which the mouse showed comparable licking rates in each pair of "laser-on" and "laser-off" trials during the anticipation period (0–3 s).

Perspectives

Our results that inhibition or activation of neurons along the aIC^{Fezf2} → NTS pathway potently suppresses or heightens, respectively, motivational vigor without influencing food or fluid consumption or affecting valence processing indicate that the function of this circuit is remarkably specialized. These results provide plausible explanations for the observations that patients with insular lesions have reduced motivational vigor or decreased addictive behaviors but have normal food intake and the pleasure of eating (Manes et al., 1999; Naqvi et al., 2014; Naqvi et al., 2007). Given that vigor is a core manifestation of motivation (Niv et al., 2007; Rigoli et al., 2016), our results also provide insights into the aIC dysfunctions linked with mood and motivational disorders (Etkin, 2010; Collins et al., 2019; Paulus and Stein, 2010; Sliz and Hayley, 2012; Sprengelmeyer et al., 2011; Stratmann et al., 2014). We propose that regulating activity in the nodes along aIC → NTS circuit could be a viable approach to achieve bidirectional and precise control of vigor and effort, and hence this circuit represents a potential therapeutic target for treating vigor- or effort-related symptoms prevalent among individuals affected by depression or drug addiction.

Limitations of study

Our *in vivo* imaging results revealed the existence of two distinct functional types among aIC^{Fezf2} or aIC^{NTS} neurons, with one exhibiting excitatory response and the other showing inhibitory response during the anticipation and consumption of homeostatically needed substances. However, our optogenetic manipulation did not discriminate between these two types and especially did not unravel the role of the neurons with inhibitory response. The recently developed technologies for simultaneous optogenetics and imaging at single-cell resolution (Emiliani et al., 2015) may prove to be useful in addressing this issue.

STAR★METHODS

Detailed methods are provided in the online version of this paper and include the following:

- KEY RESOURCES TABLE
- RESOURCE AVAILABILITY
  - ○ Lead contact
  - ○ Materials availability
  - ○ Data and code availability
- EXPERIMENTAL MODEL AND SUBJECT DETAILS

- METHOD DETAILS
  - ○ Immunohistochemistry
  - ○ Viral vectors
  - ○ Stereotaxic surgery
  - ○ Mapping monosynaptic inputs with pseudotyped rabies virus
  - ○ Tamoxifen induction
  - ○ The reward-seeking task under distinct motivational states
  - ○ Go/no-go task
  - ○ Run-for-reward task
  - ○ Progressive-ratio task
  - ○ Optogenetic activation of aIC^{Fezf2}→NTS in differing behavioral contexts
  - ○ Real-time place preference/aversion (RTPP/A) test
  - ○ Self-stimulation test
  - ○ Assessing food and liquid intake
  - ○ Continuous licking task
  - ○ Behavioral data collection and analysis
  - ○ Calcium imaging and imaging data analysis
  - ○ Evaluation of spatial clustering of neurons with specific functional properties
  - ○ Cell registration
  - ○ Analysis of aIC^{Fezf2} population dynamics in the activity space
  - ○ Population vector analysis
  - ○ Decoding analysis
  - ○ *In vivo* fiber photometry and data analysis
- QUANTIFICATION AND STATISTICAL ANALYSIS

SUPPLEMENTAL INFORMATION

Supplemental information can be found online at https://doi.org/10.1016/j.cell.2021.11.019.

(K) Left: a scatterplot of DA2m signals in pairs of laser-on and laser-off trials where the mouse had comparable anticipatory licking rates. Each dot represents such a pair. Right: quantification of the DA2m signals (*p = 0.019; Wilcoxon signed-rank test).

(L) DA2m signals in the NAc in all the ChR2 mice (n = 6) during anticipation period in the go-trials selected as those in (J, K) (t$_{(5)}$ = 6.80, **p = 0.001, paired t test).

(M and N) Licking rate (M) and DA2m signals in the NAc (N) of all the GFP mice during anticipation period (0–3 s) in different trial types. (M) F$_{(1,8)}$ = 0.73, p = 0.42; go trials, p = 0.41; no-go trials, p > 0.99. (N) F$_{(1,8)}$ = 2.02, p = 0.19; go trials, p = 0.81; no-go trials, p = 0.58. Two-way ANOVA followed by Bonferroni's test.

(O–Q) Results were obtained from the same mice as in (D)–(L), but in quenched state.

(O) Example plots showing the absence of CS-evoked licking (top) and DA2m signals in the NAc (bottom) from the same mouse as that in (D)–(G).

(P) Same as (H), except that data are from quenched state (F$_{(1,10)}$ = 0.69, p = 0.43; go trials, n.s., p = 0.20; no-go trials, n.s., p = 0.81). Two-way ANOVA followed by Bonferroni's test.

(Q) Same as (I), except that data are from quenched state (F$_{(1,10)}$ = 0.11, p = 0.74; go trials, n.s., p = 0.91; no-go trials, n.s., p = 0.99). Two-way ANOVA followed by Bonferroni's test.

Data are presented as mean ± SEM.

See also Figure S6.

REFERENCES

Allen, W.E., Chen, M.Z., Pichamoorthy, N., Tien, R.H., Pachitariu, M., Luo, L., and Deisseroth, K. (2019). Thirst regulates motivated behavior through modulation of brainwide neural population dynamics. Science *364*, 253.

Berditchevskaia, A., Cazé, R.D., and Schultz, S.R. (2016). Performance in a GO/NOGO perceptual task reflects a balance between impulsive and instrumental components of behaviour. Sci. Rep. *6*, 27389.

Berke, J.D. (2018). What does dopamine mean? Nat. Neurosci. *21*, 787–793.

Berridge, K.C., Robinson, T.E., and Aldridge, J.W. (2009). Dissecting components of reward: 'liking', 'wanting', and learning. Curr. Opin. Pharmacol. *9*, 65–73.

Bonson, K.R., Grant, S.J., Contoreggi, C.S., Links, J.M., Metcalfe, J., Weyl, H.L., Kurian, V., Ernst, M., and London, E.D. (2002). Neural systems and cue-induced cocaine craving. Neuropsychopharmacology *26*, 376–386.

Chen, X., Gabitto, M., Peng, Y., Ryba, N.J., and Zuker, C.S. (2011). A gustotopic map of taste qualities in the mammalian brain. Science *333*, 1262–1266.

Chen, T.W., Wardill, T.J., Sun, Y., Pulver, S.R., Renninger, S.L., Baohan, A., Schreiter, E.R., Kerr, R.A., Orger, M.B., Jayaraman, V., et al. (2013). Ultrasensitive fluorescent proteins for imaging neuronal activity. Nature *499*, 295–300.

Chen, X., Sun, Y.C., Zhan, H., Kebschull, J.M., Fischer, S., Matho, K., Huang, Z.J., Gillis, J., and Zador, A.M. (2019). High-Throughput Mapping of Long-Range Neuronal Projection Using In Situ Sequencing. Cell *179*, 772–786.e19.

Chen, K., Kogan, J.F., and Fontanini, A. (2021). Spatially Distributed Representation of Taste Quality in the Gustatory Insular Cortex of Behaving Mice. Curr. Biol. *31*, 247–256.e4.

Collins, I., Hänggi, J., Frei, M., Lieb, R., Holforth, M., Seifritz, E., and Spinelli, S. (2019). Insular volume reductions in patients with major depressive disorder. Neurol. Psychiatry Brain Res. *33*, 39–47.

Contreras, M., Ceric, F., and Torrealba, F. (2007). Inactivation of the interoceptive insula disrupts drug craving and malaise induced by lithium. Science *318*, 655–658.

Craig, A.D. (2009). How do you feel—now? The anterior insula and human awareness. Nat. Rev. Neurosci. *10*, 59–70.

Critchley, H.D., and Harrison, N.A. (2013). Visceral influences on brain and behavior. Neuron *77*, 624–638.

Dikecligil, G.N., Graham, D.M., Park, I.M., and Fontanini, A. (2020). Layer- and Cell Type-Specific Response Properties of Gustatory Cortex Neurons in Awake Mice. J. Neurosci. *40*, 9676–9691.

du Hoffmann, J., and Nicola, S.M. (2014). Dopamine invigorates reward seeking by promoting cue-evoked excitation in the nucleus accumbens. J. Neurosci. *34*, 14349–14364.

Emiliani, V., Cohen, A.E., Deisseroth, K., and Häusser, M. (2015). All-Optical Interrogation of Neural Circuits. J. Neurosci. *35*, 13917–13926.

Engelmann, J.M., Versace, F., Robinson, J.D., Minnix, J.A., Lam, C.Y., Cui, Y., Brown, V.L., and Cinciripini, P.M. (2012). Neural substrates of smoking cue reactivity: a meta-analysis of fMRI studies. Neuroimage *60*, 252–262.

Etkin, A. (2010). Functional neuroanatomy of anxiety: a neural circuit perspective. Curr. Top. Behav. Neurosci. *2*, 251–277.

Fenno, L.E., Mattis, J., Ramakrishnan, C., Hyun, M., Lee, S.Y., He, M., Tucciarone, J., Selimbeyoglu, A., Berndt, A., Grosenick, L., et al. (2014). Targeting cells with single vectors using multiple-feature Boolean logic. Nat. Methods *11*, 763–772.

Floresco, S.B. (2015). The nucleus accumbens: an interface between cognition, emotion, and action. Annu. Rev. Psychol. *66*, 25–52.

Forget, B., Pushparaj, A., and Le Foll, B. (2010). Granular insular cortex inactivation as a novel therapeutic strategy for nicotine addiction. Biol. Psychiatry *68*, 265–271.

Fu, Y., Yuan, Y., Halliday, G., Rusznák, Z., Watson, C., and Paxinos, G. (2012). A cytoarchitectonic and chemoarchitectonic analysis of the dopamine cell groups in the substantia nigra, ventral tegmental area, and retrorubral field in the mouse. Brain Struct. Funct. *217*, 591–612.

Gallistel, C.R., Fairhurst, S., and Balsam, P. (2004). The learning curve: implications of a quantitative analysis. Proc. Natl. Acad. Sci. USA *101*, 13124–13131.

Gao, Z., Davis, C., Thomas, A.M., Economo, M.N., Abrego, A.M., Svoboda, K., De Zeeuw, C.I., and Li, N. (2018). A cortico-cerebellar loop for motor planning. Nature *563*, 113–116.

Gogolla, N. (2017). The insular cortex. Curr. Biol. *27*, R580–R586.

Govorunova, E.G., Sineshchekov, O.A., Janz, R., Liu, X., and Spudich, J.L. (2015). NEUROSCIENCE. Natural light-gated anion channels: A family of microbial rhodopsins for advanced optogenetics. Science *349*, 647–650.

Hamid, A.A., Pettibone, J.R., Mabrouk, O.S., Hetrick, V.L., Schmidt, R., Vander Weele, C.M., Kennedy, R.T., Aragona, B.J., and Berke, J.D. (2016). Mesolimbic dopamine signals the value of work. Nat. Neurosci. *19*, 117–126.

Harris, K.D., and Mrsic-Flogel, T.D. (2013). Cortical connectivity and sensory coding. Nature *503*, 51–58.

Harris, K.D., and Shepherd, G.M. (2015). The neocortical circuit: themes and variations. Nat. Neurosci. *18*, 170–181.

He, M., Liu, Y., Wang, X., Zhang, M.Q., Hannon, G.J., and Huang, Z.J. (2012). Cell-type-based analysis of microRNA profiles in the mouse brain. Neuron *73*, 35–48.

Hodos, W. (1961). Progressive ratio as a measure of reward strength. Science *134*, 943–944.

Jin, H., Fishman, Z.H., Ye, M., Wang, L., and Zuker, C.S. (2021). Top-Down Control of Sweet and Bitter Taste in the Mammalian Brain. Cell *184*, 257–271.e16.

Katz, D.B., Simon, S.A., and Nicolelis, M.A. (2001). Dynamic and multimodal responses of gustatory cortical neurons in awake rats. J. Neurosci. *21*, 4478–4489.

Ko, D., and Wanat, M.J. (2016). Phasic Dopamine Transmission Reflects Initiation Vigor and Exerted Effort in an Action- and Region-Specific Manner. J. Neurosci. *36*, 2202–2211.

Kühn, S., and Gallinat, J. (2011). Common biology of craving across legal and illegal drugs - a quantitative meta-analysis of cue-reactivity brain response. Eur. J. Neurosci. *33*, 1318–1326.

Kusumoto-Yoshida, I., Liu, H., Chen, B.T., Fontanini, A., and Bonci, A. (2015). Central role for the insular cortex in mediating conditioned responses to anticipatory cues. Proc. Natl. Acad. Sci. USA *112*, 1190–1195.

Lee, W., and Reeve, J. (2013). Self-determined, but not non-self-determined, motivation predicts activations in the anterior insular cortex: an fMRI study of personal agency. Soc. Cogn. Affect. Neurosci. *8*, 538–545.

Lee, W., and Reeve, J. (2017). Identifying the neural substrates of intrinsic motivation during task performance. Cogn. Affect. Behav. Neurosci. *17*, 939–953.

Lee, S., Augustine, V., Zhao, Y., Ebisu, H., Ho, B., Kong, D., and Oka, Y. (2019). Chemosensory modulation of neural circuits for sodium appetite. Nature *568*, 93–97.

Li, N., Daie, K., Svoboda, K., and Druckmann, S. (2016). Robust neuronal dynamics in premotor cortex during motor planning. Nature *532*, 459–464.

Livneh, Y., Ramesh, R.N., Burgess, C.R., Levandowski, K.M., Madara, J.C., Fenselau, H., Goldey, G.J., Diaz, V.E., Jikomes, N., Resch, J.M., et al. (2017). Homeostatic circuits selectively gate food cue responses in insular cortex. Nature *546*, 611–616.

Livneh, Y., Sugden, A.U., Madara, J.C., Essner, R.A., Flores, V.I., Sugden, L.A., Resch, J.M., Lowell, B.B., and Andermann, M.L. (2020). Estimation of Current and Future Physiological States in Insular Cortex. Neuron *105*, 1094–1111.e10.

Lodato, S., Molyneaux, B.J., Zuccaro, E., Goff, L.A., Chen, H.H., Yuan, W., Meleski, A., Takahashi, E., Mahony, S., Rinn, J.L., et al. (2014). Gene co-regulation by Fezf2 selects neurotransmitter identity and connectivity of corticospinal neurons. Nat. Neurosci. *17*, 1046–1054.

Luijten, M., Veltman, D.J., van den Brink, W., Hester, R., Field, M., Smits, M., and Franken, I.H. (2011). Neurobiological substrate of smoking-related attentional bias. Neuroimage *54*, 2374–2381.

Maffei, A., Haley, M., and Fontanini, A. (2012). Neural processing of gustatory information in insular circuits. Curr. Opin. Neurobiol. *22*, 709–716.

Mahn, M., Gibor, L., Patil, P., Cohen-Kashi Malina, K., Oring, S., Printz, Y., Levy, R., Lampl, I., and Yizhar, O. (2018). High-efficiency optogenetic silencing with soma-targeted anion-conducting channelrhodopsins. Nat. Commun. *9*, 4125.

Manes, F., Paradiso, S., and Robinson, R.G. (1999). Neuropsychiatric effects of insular stroke. J. Nerv. Ment. Dis. *187*, 707–712.

Matho, K.S., Huilgol, D., Galbavy, W., He, M., Kim, G., An, X., Lu, J., Wu, P., Di Bella, D.J., Shetty, A.S., et al. (2021). Genetic dissection of the glutamatergic neuron system in cerebral cortex. Nature *598*, 182–187.

Menon, V., and Uddin, L.Q. (2010). Saliency, switching, attention and control: a network model of insula function. Brain Struct. Funct. *214*, 655–667.

Mohebi, A., Pettibone, J.R., Hamid, A.A., Wong, J.T., Vinson, L.T., Patriarchi, T., Tian, L., Kennedy, R.T., and Berke, J.D. (2019). Dissociable dopamine dynamics for learning and motivation. Nature *570*, 65–70.

Naqvi, N.H., Rudrauf, D., Damasio, H., and Bechara, A. (2007). Damage to the insula disrupts addiction to cigarette smoking. Science *315*, 531–534.

Naqvi, N.H., Gaznick, N., Tranel, D., and Bechara, A. (2014). The insula: a critical neural substrate for craving and drug seeking under conflict and risk. Ann. N Y Acad. Sci. *1316*, 53–70.

Niv, Y., Daw, N.D., Joel, D., and Dayan, P. (2007). Tonic dopamine: opportunity costs and the control of response vigor. Psychopharmacology (Berl.) *191*, 507–520.

Paton, J.J., Belova, M.A., Morrison, S.E., and Salzman, C.D. (2006). The primate amygdala represents the positive and negative value of visual stimuli during learning. Nature *439*, 865–870.

Paulus, M.P., and Stein, M.B. (2010). Interoception in anxiety and depression. Brain Struct. Funct. *214*, 451–463.

Peng, Y., Gillis-Smith, S., Jin, H., Tränkner, D., Ryba, N.J., and Zuker, C.S. (2015). Sweet and bitter taste in the brain of awake behaving animals. Nature *527*, 512–515.

Pnevmatikakis, E.A., Soudry, D., Gao, Y., Machado, T.A., Merel, J., Pfau, D., Reardon, T., Mu, Y., Lacefield, C., Yang, W., et al. (2016). Simultaneous Denoising, Deconvolution, and Demixing of Calcium Imaging Data. Neuron *89*, 285–299.

Quadt, L., Critchley, H.D., and Garfinkel, S.N. (2018). The neurobiology of interoception in health and disease. Ann. N Y Acad. Sci. *1428*, 112–128.

Reardon, T.R., Murray, A.J., Turi, G.F., Wirblich, C., Croce, K.R., Schnell, M.J., Jessell, T.M., and Losonczy, A. (2016). Rabies Virus CVS-N2c(ΔG) Strain Enhances Retrograde Synaptic Transfer and Neuronal Viability. Neuron *89*, 711–724.

Richardson, N.R., and Roberts, D.C. (1996). Progressive ratio schedules in drug self-administration studies in rats: a method to evaluate reinforcing efficacy. J. Neurosci. Methods *66*, 1–11.

Rigoli, F., Chew, B., Dayan, P., and Dolan, R.J. (2016). The Dopaminergic Midbrain Mediates an Effect of Average Reward on Pavlovian Vigor. J. Cogn. Neurosci. *28*, 1303–1317.

Rozeske, R.R., Jercog, D., Karalis, N., Chaudun, F., Khoder, S., Girard, D., Winke, N., and Herry, C. (2018). Prefrontal-Periaqueductal Gray-Projecting Neurons Mediate Context Fear Discrimination. Neuron *97*, 898–910.e6.

Samuelsen, C.L., and Fontanini, A. (2017). Processing of Intraoral Olfactory and Gustatory Signals in the Gustatory Cortex of Awake Rats. J. Neurosci. *37*, 244–257.

Samuelsen, C.L., Gardner, M.P.H., and Fontanini, A. (2012). Effects of cue-triggered expectation on cortical processing of taste. Neuron *74*, 410–422.

Sheintuch, L., Rubin, A., Brande-Eilat, N., Geva, N., Sadeh, N., Pinchasof, O., and Ziv, Y. (2017). Tracking the Same Neurons across Multiple Days in Ca^{2+} Imaging Data. Cell Rep. *21*, 1102–1115.

Shipley, M.T. (1982). Insular cortex projection to the nucleus of the solitary tract and brainstem visceromotor regions in the mouse. Brain Res. Bull. *8*, 139–148.

Shuvaev, S.A., Tran, N.B., Stephenson-Jones, M., Li, B., and Koulakov, A.A. (2021). Neural Networks With Motivation. Front. Syst. Neurosci. *14*, 609316.

Sliz, D., and Hayley, S. (2012). Major depressive disorder and alterations in insular cortical activity: a review of current functional magnetic imaging research. Front. Hum. Neurosci. *6*, 323.

Sprengelmeyer, R., Steele, J.D., Mwangi, B., Kumar, P., Christmas, D., Milders, M., and Matthews, K. (2011). The insular cortex and the neuroanatomy of major depression. J. Affect. Disord. *133*, 120–127.

Stephenson-Jones, M., Bravo-Rivera, C., Ahrens, S., Furlan, A., Xiao, X., Fernandes-Henriques, C., and Li, B. (2020). Opposing Contributions of GABAergic and Glutamatergic Ventral Pallidal Neurons to Motivational Behaviors. Neuron *105*, 921–933.e5.

Stratmann, M., Konrad, C., Kugel, H., Krug, A., Schöning, S., Ohrmann, P., Uhlmann, C., Postert, C., Suslow, T., Heindel, W., et al. (2014). Insular and hippocampal gray matter volume reductions in patients with major depressive disorder. PLoS ONE *9*, e102692.

Sun, F., Zeng, J., Jing, M., Zhou, J., Feng, J., Owen, S.F., Luo, Y., Li, F., Wang, H., Yamaguchi, T., et al. (2018). A Genetically Encoded Fluorescent Sensor Enables Rapid and Specific Detection of Dopamine in Flies, Fish, and Mice. Cell *174*, 481–496.e19.

Sun, F., Zhou, J., Dai, B., Qian, T., Zeng, J., Li, X., Zhuo, Y., Zhang, Y., Wang, Y., Qian, C., et al. (2020). Next-generation GRAB sensors for monitoring dopaminergic activity in vivo. Nat. Methods *17*, 1156–1166.

Suter, B.A., Migliore, M., and Shepherd, G.M. (2013). Intrinsic electrophysiology of mouse corticospinal neurons: a class-specific triad of spike-related properties. Cereb. Cortex *23*, 1965–1977.

Tasic, B., Yao, Z., Graybuck, L.T., Smith, K.A., Nguyen, T.N., Bertagnolli, D., Goldy, J., Garren, E., Economo, M.N., Viswanathan, S., et al. (2018). Shared and distinct transcriptomic cell types across neocortical areas. Nature *563*, 72–78.

Tindell, A.J., Smith, K.S., Berridge, K.C., and Aldridge, J.W. (2009). Dynamic computation of incentive salience: "wanting" what was never "liked". J. Neurosci. *29*, 12220–12228.

Venniro, M., Caprioli, D., Zhang, M., Whitaker, L.R., Zhang, S., Warren, B.L., Cifani, C., Marchant, N.J., Yizhar, O., Bossert, J.M., et al. (2017). The Anterior Insular Cortex→Central Amygdala Glutamatergic Pathway Is Critical to Relapse after Contingency Management. Neuron *96*, 414–427.e8.

Vincis, R., and Fontanini, A. (2016). A gustocentric perspective to understanding primary sensory cortices. Curr. Opin. Neurobiol. *40*, 118–124.

Wang, L., Gillis-Smith, S., Peng, Y., Zhang, J., Chen, X., Salzman, C.D., Ryba, N.J.P., and Zuker, C.S. (2018). The coding of valence and identity in the mammalian taste system. Nature *558*, 127–131.

Wu, Y., Chen, C., Chen, M., Qian, K., Lv, X., Wang, H., Jiang, L., Yu, L., Zhuo, M., and Qiu, S. (2020). The anterior insular cortex unilaterally controls feeding in response to aversive visceral stimuli in mice. Nat. Commun. *11*, 640.

Xiao, X., Deng, H., Furlan, A., Yang, T., Zhang, X., Hwang, G.R., Tucciarone, J., Wu, P., He, M., Palaniswamy, R., et al. (2020). A Genetically Defined Compartmentalized Striatal Direct Pathway for Negative Reinforcement. Cell *183*, 211–227.e20.

Yao, Z., van Velthoven, C.T.J., Nguyen, T.N., Goldy, J., Sedeno-Cortes, A.E., Baftizadeh, F., Bertagnolli, D., Casper, T., Chiang, M., Crichton, K., et al. (2021). A taxonomy of transcriptomic cell types across the isocortex and hippocampal formation. Cell *184*, 3222–3241.e26.

Zhang, X., and Li, B. (2018). Population coding of valence in the basolateral amygdala. Nat. Commun. *9*, 5195.

Zhang, X., Guan, W., Yang, T., Furlan, A., Xiao, X., Yu, K., An, X., Galbavy, W., Ramakrishnan, C., Deisseroth, K., et al. (2021). Genetically identified amygdala-striatal circuits for valence-specific behaviors. Nat. Neurosci. *24*, 1586–1600.

Zhou, P., Resendez, S.L., Rodriguez-Romaguera, J., Jimenez, J.C., Neufeld, S.Q., Giovannucci, A., Friedrich, J., Pnevmatikakis, E.A., Stuber, G.D., Hen, R., et al. (2018). Efficient and accurate extraction of in vivo calcium signals from microendoscopic video data. eLife *7*, e28728.

Zingg, B., Chou, X.L., Zhang, Z.G., Mesik, L., Liang, F., Tao, H.W., and Zhang, L.I. (2017). AAV-Mediated Anterograde Transsynaptic Tagging: Mapping Corticocollicular Input-Defined Neural Pathways for Defense Behaviors. Neuron *93*, 33–47.

STAR★METHODS

KEY RESOURCES TABLE

REAGENT or RESOURCE	SOURCE	IDENTIFIER
Antibodies		
Chicken polyclonal anti-GFP	Aves Labs	Cat# GFP1020; RRID:AB_10000240
Rabbit polyclonal anti-RFP	Rockland	Cat# 600-401-379; RRID:AB_2209751
Rabbit polyclonal anti-tyrosine hydroxylase	Millipore	Cat# AB152; RRID:AB_390204
Bacterial and virus strains		
AAV5-Ef1a-DIO-hChR2(H134R)-eYFP	UNC Vector Core	N/A
AAV9-CAG-Flex-GFP	UNC Vector Core	N/A
AAV1-Syn-Flex-GCaMP6f-WPRE-SV40	Chen et al., 2013	Addgene 100833
AAV1-hSyn-SIO-stGtACR2-FusionRed	Mahn et al., 2018	Addgene 105677
AAV-Ef1a-mCherry-IRES-Cre (retrograde)	Fenno et al., 2014	Addgene 55632
AAV1-hSyn-Cre-WPRE-hGh	Penn Vector Core	N/A
AAV9-hSyn-DA2m	Vigene Biosciences	N/A
AAV2/9-CAG-Flex-mKate-T2A-TVA	HHMI Janelia Research Campus	N/A
AAV2/9-CAG-Flex-mKate-T2A-N2c-G	HHMI Janelia Research Campus	N/A
Rbv-CVS-N2c-ΔG-GFP	HHMI Janelia Research Campus	Addgene 73461
Experimental models: Organisms/strains		
Mouse: Fezf2-2A-CreER	Matho et al., 2021	JAX stock# 036296
Mouse: Rosa26-loxp-STOP-loxp-H2B-GFP	He et al., 2012	N/A
Software and algorithms		
ImageJ (Fiji) software	NIH	https://fiji.sc/
MATLAB	Mathworks	https://www.mathworks.com/products/matlab.html
GraphPad Prism 7	GraphPad Software	https://www.graphpad.com/
Original code	This paper	https://figshare.com/articles/software/Codes_for_insular-NTS_paper/16915519

RESOURCE AVAILABILITY

Lead contact
Further information and requests for resources and reagents should be directed to and will be fulfilled by the Lead Contact, Bo Li (bli@cshl.edu).

Materials availability
This study did not generate new unique reagents.

Data and code availability
- The authors declare that the data supporting the findings of this study are available within the paper and its supplementary information files.
- All original code has been deposited at Figshare and is publicly available as of the date of publication. DOIs are listed in the Key Resources Table.
- Any additional information required to reanalyze the data reported in this paper is available from the lead contact upon request.

EXPERIMENTAL MODEL AND SUBJECT DETAILS

Male and female mice (2-4 months old) were used for all the experiments. All mice were bred onto a C57BL/6J background. Mice were housed in groups of 2-5 under a 12 h light/dark cycle (8 a.m. to 8 p.m. light), with food and water available *ad libitum* before

being used for experiments. All behavioral experiments were conducted during the light cycle. Littermates were randomly assigned to different groups prior to experiments. All experimental procedures were approved by the Institutional Animal Care and Use Committee of Cold Spring Harbor Laboratory (CSHL) and performed in accordance to the US National Institutes of Health guidelines in an AAALACi accredited facility.

The *Fezf2-CreER* knock-in (Matho et al., 2021) and *H2B-GFP* (*Rosa26-stop^flox^-H2B-GFP*) reporter (He et al., 2012) mouse lines were generated by Z. Josh Huang's lab at CSHL.

METHOD DETAILS

Immunohistochemistry

Immunohistochemistry experiments were performed following standard procedures described previously (Xiao et al., 2020). Briefly, mice were anesthetized with Euthasol (0.2 ml; Virbac, Fort Worth, Texas, USA) and transcardially perfused with 30 mL PBS, followed by 30 mL 4% paraformaldehyde (PFA) in PBS. Brains were extracted and further fixed in 4% PFA overnight followed by cryoprotection in a 30% PBS-buffered sucrose solution for 36-48 h at 4°C. Coronal sections (50 μm) were cut using a freezing microtome (Leica SM 2010R, Leica). Sections were first washed in PBS (5 min), incubated in PBST (0.3% Triton X-100 in PBS) for 30 min at room temperature (RT) and then washed with PBS (3 × 5 min). Next, sections were blocked in 5% normal goat serum in PBST for 30 min at RT and then incubated with primary antibodies overnight at 4°C. Sections were washed with PBS (3 × 5 min) and incubated with fluorescent secondary antibodies at RT for 2 h. In some experiments (as indicated in Figures and Supplementary Figures), sections were washed twice in PBS, incubated with DAPI (4′,6-diamidino-2-phenylindole, Invitrogen, catalog number D1306) (0.5μg/ml in PBS) for 2 min. After washing with PBS (3 × 5 min), sections were mounted onto slides with Fluoromount-G (eBioscience, San Diego, California, USA). Images were taken using an LSM 780 laser-scanning confocal microscope (Carl Zeiss, Oberkochen, Germany). The primary antibodies used were: chicken anti-GFP (Aves Labs, catalog number GFP1020; dilution 1:1000), rabbit anti-RFP (Rockland, catalog number 600-401-379; dilution 1:1000), rabbit anti-tyrosine hydroxylase (TH) (Millipore, catalog number AB152; dilution 1:1000). Appropriate fluorophore-conjugated secondary antibodies (Life Technologies) were used depending on the desired fluorescence colors.

Viral vectors

The following adeno-associated viruses (AAVs) were produced by the University of North Carolina vector core facility (Chapel Hill, North Carolina, USA): AAV5-Ef1a-DIO-hChR2(H134R)-eYFP, AAV9-CAG-Flex-GFP. The AAV1-Syn-Flex-GCaMP6f-WPRE-SV40, AAV1-hSyn-SIO-stGtACR2-FusionRed and AAV-Ef1a-mCherry-IRES-Cre (retrograde) (Fenno et al., 2014) were produced by Addgene (Watertown, MA, USA). The AAV1-hSyn-Cre-WPRE-hGh (anterograde *trans*-synaptic) was packaged by UPenn Vector Core (Philadelphia, PA, USA). The AAV9-hSyn-DA2m was packaged by Vigene Biosciences (Rockville, MD, USA). The following viruses, which are components of the rabies viral tracing system, were produced by HHMI Janelia Research Campus: AAV2/9-CAG-Flex-mKate-T2A-TVA, AAV2/9-CAG-Flex-mKate-T2A-N2c-G, Rbv-CVS-N2c-ΔG-GFP (the modified rabies virus). All viral vectors were aliquoted and stored at −80°C until use.

Stereotaxic surgery

All surgery was performed under aseptic conditions and body temperature was maintained with a heating pad. Standard surgical procedures were used for stereotaxic injection and implantation as previously described (Xiao et al., 2020). Briefly, mice were anesthetized with isoflurane (1%–2% in a mixture with oxygen, applied at 1.0 L/min), and head-fixed in a stereotaxic injection frame, which was linked to a digital mouse brain atlas to guide the targeting of different brain structures (Angle Two Stereotaxic System, myNeuroLab.com). Lidocaine was injected subcutaneously into the head and neck area as a local anesthetic.

We first made a small cranial window (1-2 mm²) above the target brain region. To prepare mice for the GRIN lens imaging experiments, we lowered a glass micropipette (tip diameter, ~5 μm) containing the AAV1-Syn-Flex-GCaMP6f-WPRE-SV40 viral solution to reach the aIC at two dorsoventral positions (coordinates: 1.6 mm anterior to Bregma, 3.1 mm lateral from midline, 1.9 mm and 2.1 mm vertical from brain surface). About 0.25 μL of viral solution was delivered at each injection site (in total 0.5 μl) with pressure applications (5-20 psi, 5-20 ms at 1 Hz) controlled by a Picospritzer III (General Valve) and a pulse generator (Agilent). The rate of injection was ~20 nl/min. The pipette was left in place for 10 min following the injection, and then slowly withdrawn. In the experiment to image NTS-projecting aIC (aIC^NTS) neurons, we additionally injected the AAV-Ef1a-mCherry-IRES-Cre (retrograde) into the NTS (coordinates: 6.55 mm posterior to Bregma, 1.37 mm lateral from midline, and 3.8 mm vertical from brain surface). One week later, we performed the second surgery to implant a GRIN lens (diameter, 0.6 mm; length, 7.3 mm; Inscopix). The lens was slowly (~100 μm/min) lowered to the aIC (coordinates: 1.6 mm anterior to Bregma, 3.1 mm lateral from midline, 1.7 mm vertical from brain surface), and subsequently secured to the skull by using C&B-Metabond (Parkell, catalog number S380). A metal head-bar (for head restraint) was then mounted onto the skull with black dental cement (Ortho-Jet). We waited for ~4 weeks before starting the imaging experiments in these mice.

To prepare mice for the optogenetic experiments, we first injected the targets in both hemispheres with viruses, and subsequently implanted optic fibers above the injection locations or axon terminal fields. A head-bar was also mounted for head restraint. Viruses were injected at a volume of ~0.3 μl at each site, and were allowed ~4 weeks for expression. Viral injection was performed at the

following stereotaxic coordinates for the aIC: 1.6 mm anterior to Bregma, 3.1 mm lateral from midline, 2.0 mm ventral from cortical surface; NTS: 6.55 mm posterior to Bregma, 1.37 mm lateral from midline, 3.8 mm ventral from cortical surface. Coordinates for optic fiber implantation were as follows: aIC: 1.6 mm anterior to Bregma, 3.1 mm lateral from midline, 1.65 mm ventral from cortical surface; NTS: 6.55 mm posterior to Bregma, 1.5 mm lateral from midline, 3.6 mm ventral from cortical surface with a 3° angle; and PBN: 5.3 mm posterior to Bregma, 1.9 mm lateral from midline, 2.2 mm ventral from cortical surface with a 14.85° angle. The optic fibers (core diameter, 200 μm; length, 3 mm (for aIC and PBN) or 4.5 mm (for NTS); NA, 0.22; Newdoon, Hangzhou, China; or Inper, Hangzhou, China) used for the photostimulation transmitted light with > 90% efficiency when tested before implantation.

To monitor the neural activity of NTS neurons receiving inputs from aIC (the NTS^{Recipient}) using fiber photometry, we injected the aIC with ∼0.3 μl of the anterograde *trans*-synaptic AAV1-hSyn-Cre-WPRE-hGh, and injected the NTS with ∼0.3 μl of AAV1-Syn-Flex-GCaMP6f-WPRE-SV40 at the coordinates described above. An optic fiber (core diameter, 200 μm; length, 4.5 mm; NA, 0.37; Newdoon, Hangzhou, China; or Inper, Hangzhou, China) was inserted 0.2 mm above the injection site in the NTS.

For the *in vivo* opto-photometry experiment, *Fezf2-CreER* mice were injected with ∼0.3 μl AAV5-Ef1a-DIO-hChR2(H134R)-eYFP into the aIC and ∼0.3 μl AAV9-hSyn-DA2m into the NAc core (coordinates: 1.3 mm anterior to Bregma, 0.8 mm lateral from midline, 3.8 mm ventral from cortical surface). Optical fibers for photoactivation were implanted in the NTS at coordinates described above. Optical fibers for fiber photometry were implanted 0.2 mm above the injection site in the NAc.

To retrogradely label PBN- and NTS-projecting neurons in the IC of the same mice, we unilaterally injected ∼0.2 μl CTB-555 solution (0.1% in PBS) into the PBN (coordinates: 5.3 mm posterior to Bregma, 1.9 mm lateral from midline, 2.63 mm ventral from cortical surface with a 14.85° angle) and ∼0.2 μl CTB-647 solution (0.1% in PBS) into the NTS in C57BL/6J mice. Mice were sacrificed 5 days after the injection to allow retrograde labeling of projection neurons.

For anterograde tracing of aIC^{Fezf2} neurons, we unilaterally injected ∼0.2 μl of AAV9-CAG-Flex-GFP into the aIC in *Fezf2-CreER* mice. For anterograde tracing of NTS^{Recipient} neurons, ∼0.3 μl of AAV1-hSyn-Cre-WPRE-hGh was injected into the aIC, and ∼0.3 μl of AAV9-CAG-Flex-GFP was injected into the NTS. We waited about 3-4 weeks before perfusing the mice.

Mapping monosynaptic inputs with pseudotyped rabies virus

Retrograde tracing of monosynaptic inputs onto aIC^{Fezf2} neurons was accomplished using a previously described method (Reardon et al., 2016; Xiao et al., 2020; Zhang et al., 2021). We first injected the aIC of *Fezf2-CreER* mice with a mixture of AAV-Flex-mKate-T2A-TVA and AAV-Flex-mKate-T2A-N2c-G (1:2 volume: volume ratio; ∼0.3 μl in total) that express the following components in a Cre-dependent manner: a fluorescent reporter mKate, TVA (which is a receptor for the avian virus envelope protein EnvA), and the rabies envelope glycoprotein (G). Three weeks later, mice were injected in the same location with Rbv-CVS-N2c-ΔG-GFP (∼0.3 μl), a rabies virus that is pseudotyped with EnvA, lacks the envelope glycoprotein, and expresses GFP. This rabies strain has been shown to have enhanced retrograde *trans*-synaptic transfer and reduced neurotoxicity (Reardon et al., 2016). Brain tissue was prepared one week after the rabies virus injection for histological examination. This method ensures that the rabies virus exclusively infects cells expressing TVA. Furthermore, complementation of the modified rabies virus with the envelope glycoprotein in the TVA-expressing cells allows the generation of infectious particles, which then can *trans*-synaptically infect presynaptic neurons.

Tamoxifen induction

All *Fezf2-CreER* mice underwent tamoxifen induction to activate the Cre-dependent expression of genes of interest. Tamoxifen (Sigma-Aldrich, catalog number T5648) was dissolved in corn oil at a concentration of 20 mg/ml, by constant shaking for 24 hours at room temperature in a container protected from light. Aliquots (1 mL each) were stored at 4°C. Tamoxifen induction was performed via intraperitoneal injection at a dose of 0.1 mg/g of body weight, once every 2 days for a total of 3 times. For virally driven gene expression, the first induction was performed one day after surgery. All mice were closely monitored throughout the course of tamoxifen injections and the post-injection period.

The reward-seeking task under distinct motivational states

Thirsty mice were trained to perform a reward-seeking task, in which a sound (CS, 1 s in duration) predicted that a 200-mM sucrose solution (US) would be available for the mice to consume from a spout, but only if the mice licked the spout during a response window (2 s in duration) following CS presentation. Such trials were counted as "hit" trials. To assess how changes in thirst state influence behavioral and neural activity, we first conducted one session of the imaging experiment on mice performing the task in a thirsty state. Each mouse acquired 8 μl of the sucrose solution in every hit trial. At the end of the first session, we provided each of the mice with 2 mL of the sucrose solution. We then conducted a second session of imaging on these mice (which were all quenched).

To assess how reward size affects behavioral and neural activity, we performed the imaging experiment on thirsty mice performing the task in two blocks of trials in each session. In one block, a big reward (12 μl of sucrose solution) was delivered in each hit trial; in the other block, a small reward (3 μl of sucrose solution) was delivered in each hit trial. The same CS was used in both blocks. The sequence of the blocks was counterbalanced in different sessions.

To assess how sodium deficiency affects behavioral and neural activity, we induced a sodium-depletion state in the mice, and used a high concentration (500 mM) of NaCl solution instead of the sucrose solution as the US in the reward-seeking task. To induce the sodium-depletion state, furosemide (Sigma, catalog number F4381) was administered to mice via intraperitoneal injection (50 mg/kg of body weight), as previously described (Lee et al., 2019; Tindell et al., 2009). The mice were subsequently placed on a

sodium-deficient diet (Bio-serv, catalog number F7730) and had free access to distilled water. These mice were trained to lick for the NaCl solution in the reward-seeking task. We conducted one session of imaging on these mice performing the task. Each mouse acquired 5 μl of the NaCl solution in every hit trial. After this experiment, the mice were allowed to recover for at least 4 days on a normal diet. We conducted a second session of imaging on these mice after the recovery.

Go/no-go task

Water restricted mice were trained in an auditory go/no-go task under head restraint, as previously described (Xiao et al., 2020). Training started with habituation, during which mice received water reward by licking the water spout (2 μl for each lick). No auditory stimulus was presented. Once mice reliably licked the spout (for 2-3 days), they were subjected to the go/no-go training that included "go trials" and "no-go trials." In go trials, an auditory stimulus (the "go tone," 1 s in duration) was delivered, followed by a delay period (the "response window," 1 s duration in optogenetics experiments and 2 s duration in imaging experiments). Licking during the response window was rewarded with a drop (5 μl) of a 200-mM sucrose solution. In no-go trials, a different auditory stimulus (the "no-go tone," 1 s) was delivered, followed by a response window (same duration as that in go trials). Licking during the response window resulted in the delivery of a drop (5 μl) of a 5-mM quinine solution. The go trials and no-go trials were randomly interleaved. During the inter-trial interval, brief suction (500 ms in duration) near the spout was applied to remove any residual solution from the previous trial. For analysis, trials were sorted into go trials and no-go trials. In the optogenetics experiments, trials were further sorted into laser-on and laser-off trials. Laser illumination was delivered during the time window from tone onset to US onset in 20% of randomly selected trials. The laser illumination was 10 mW measured at the tip of optic fibers. For optogenetic activation, the laser pulses were 20 Hz with a 10-ms pulse width. For optogenetic inhibition, continuous illumination was applied. A correct response during a go trial ("hit") occurred when the mouse successfully licked the spout during the response window and subsequently received the sucrose. A correct response during a no-go trial ("correct rejection") occurred when the mouse successfully withheld lick response during the response window and thus avoided the delivery of quinine. Licking in no-go trials (false alarm, FA) resulted in the delivery of quinine. The performance was quantified as hit rate (number of hits / number of go trials) and correct rejection rate (number of correct rejections / number of no-go trials). Behavioral d-prime (*d′*) was computed as follows:

$$d' = norminv(P_{Hit}) - norminv(P_{FA})$$

where *norminv* is the inverse of the cumulative normal function. Values of Hit and FA rate were truncated between 0.01 and 0.99, setting the maximum d' to 4.65.

Run-for-reward task

This task was designed to train mice to actively run on a wheel to pursue reward. Mice were first habituated to running on a wheel under head-restraint for 2-4 days (one session per day, each lasting 30∼45 min). Mice were subsequently subjected to training in which they were presented with a 1 s 3-kHz tone followed by a 1 s response window. If mice ran above a threshold speed (8 cm/s) during the response window, they would receive 8 μL of water delivered through a spout. Such trials were counted as "hit" trials. Otherwise mice would receive nothing. Mice were trained one session per day. The inter-trial interval was randomly variable between 10 to 16 s.

Progressive-ratio task

Water restricted mice were placed in a chamber equipped with a water port. Mice were first trained to poke into the port for water reward on a "fixed ratio 1" (FR1) schedule for 2 days, during which every nose-poke leads to a reward (5 μl of water). Following the FR1 training, the schedule was changed to FR4 for 2 days, which required the mice to poke the port 4 times with a maximal inter-poke-interval of 2 minutes in order to receive the reward. Next, the schedule was changed to FR10 for 1 day. Finally, mice were tested with a progressive ratio (PR) schedule in which the number of nose-pokes required to obtain one reward followed a geometric progression according to a function:

$$N_j = 20e^{j/20} - 20$$

where j is the trial number. The function was modified on the basis of previous studies (Hodos, 1961; Richardson and Roberts, 1996). Before the PR schedule, mice were tested in an FR10 session. For the optogenetic activation during PR, mice received 10 Hz photo-stimulation (10-ms pulses; 4 s laser on periods with 2 s laser off intervals; power, 10 mW; λ = 473 nm) during the entire PR session (60 min).

Optogenetic activation of aIC^{Fezf2}→NTS in differing behavioral contexts

The structure of the task in each session is similar to that of the reward-seeking task described above. In each trial of the task, a sound (CS, 1 s in duration) was presented, followed by a response window (1 s in duration). Licking during the response window led to distinct outcomes in different sessions. In each training session, water-restricted mice were trained to lick during the response window to obtain one of the following outcomes: water, 200 mM sucrose, 300 mM NaCl, or 5 mM quinine. Mice obtained 8 μL of the respective solution in each hit trial. In the test session, mice were first presented with 30 trials to remind them of the specific outcome,

then tested with photoactivation of aIC^{Fezf2}→NTS pathway in 20% of randomly selected trials. The photoactivation was applied in the time window between CS onset and US onset (λ = 473 nm; power, 10 mW measured at the tip of optic fibers; 20 Hz with a 10-ms pulse width). For the extinction session, previously well-trained mice received extinction training in which licking during the response window no longer resulted in any outcome. For the quenched condition, well-trained mice were given free access to water before the test and then tested in a session where water was the outcome. For the test with Ensure (Ensure Original Nutrition Powder, Abbott), mice were food restricted to 85% of free-feeding body weight, and then tested in a session where Ensure was the outcome (10 μL (0.015 calories) on each hit).

Real-time place preference/aversion (RTPP/A) test
Freely moving mice were initially habituated to a two-sided chamber (23 × 33 × 25 cm; made from Plexiglas) for 10 min, during which their baseline preference for the left or right side of the chamber was assessed. During the first test session (10 min), we assigned one side of the chamber (counterbalanced across mice) as the photostimulation side, and placed the mice in the non-stimulation side to start the experiment. Once the mouse entered the stimulation side, photostimulation, generated by a 473 nm laser (Shanghai Laser & Optics Century, Shanghai, China), was immediately turned on, and was turned off as soon as the mouse exited the stimulation side. In the second test session (10 min) we repeated this procedure but assigned the other side of the chamber as the stimulation side. For optogenetic activation, the photostimulation parameters were 10-ms pulse width, 20-Hz frequency, 10-mW power measured at fiber tips. For optogenetic inhibition, the photostimulation was 10-mW constant illumination. The mice were videotaped during the test with a CCD camera interfaced with Ethovision software (Noldus Information Technologies), which was also used to control the laser stimulation and extract behavioral parameters (position, time, distance and velocity).

Self-stimulation test
Freely moving mice were placed in a chamber equipped with two ports. Poking nose into one of the ports (the active port) triggered photostimulation (10-ms pulses, 20 Hz, 10 mW; λ = 473 nm) for 2 s in the NTS, whereas poking into the other port (the inactive port) did not trigger photostimulation. Mice were allowed to freely poke the two ports in 1-hour sessions, with the designation of active port in each session being counterbalanced.

Assessing food and liquid intake
Food or liquid intake was assessed in the home cage, where mice were individually housed. Mice were first food or water deprived for 24 hours. Their subsequent food or water intake in a 1-hour period was assessed. For optogenetic activation in this experiment, the photostimulation was 4 s trains of light pulses (10-ms pulse width, 20-Hz frequency, and 10-mW power measured at optical fiber tips) interleaved with 4 s light-off intervals. For optogenetic inhibition, the photostimulation was 4 s constant light illumination (10 mW) periods interleaved with 4 s light-off intervals. The light was generated by a 473 nm laser (Shanghai Laser & Optics Century, Shanghai, China). Experiments were conducted during the light-cycle, between 1 p.m. and 6 p.m.

To monitor liquid intake at a finer temporal resolution, we trained thirsty mice to obtain sucrose solution from a bottle in a chamber. These mice were subsequently tested in sessions containing laser-on and laser-off blocks. Each session contained 3 laser-off blocks and 3 laser-on blocks, with each block lasting 3 min. Each session started from either a laser-on or a laser-off block, with the two types of blocks interleaved with each other. For optogenetic activation in the light-on blocks, the photostimulation parameters were 10-ms pulse width, 20-Hz frequency, 10-mW power. For optogenetic inhibition in the light-on blocks, the photostimulation was constant light illumination (10-mW power). The light was generated by a 473 nm laser (Shanghai Laser & Optics Century, Shanghai, China).

Continuous licking task
Water deprived mice were trained to lick a spout to obtain a sucrose solution (200 mM). Each lick triggered the delivery of 0.3 μL of the solution. It took mice 4-7 days to achieve stable licking, the criterion of which was 10-min of continuous licking without any gap longer than 10 s. The mice were subsequently tested in the optogenetic manipulation experiments.

Behavioral data collection and analysis
Stimulus playback and trial control were performed via a Bpod/PulsePal open-source Arduino-based system (Sanworks, Stony Brook, NY, USA). Custom-written scripts in MATLAB based on Bpod commands were used to control the delivery of CS and US and record behavioral responses, including licking events, poking events and running velocity. Pure tones (70 dB; the CS) with different frequencies were generated as sine wave. The tones were uploaded to the audio adaptor board using the Bpod control system. The amount of liquid (the US) was controlled by fast solenoid valves (Lee Company). A metal spout was placed in front of the mouth of an animal for liquid delivery. In experiments which required delivery of sucrose and quinine, we used two tubes (one for each solution) epoxied together to avoid mixing of tastants. The spout also served as part of a custom "lickometer" circuit, which registered a lick event each time a mouse completed the circuit by licking the spout. The licking events were recorded and analyzed using custom scripts written in MATLAB. We used a rotary encoder (YUMO-E6B2-CWZ3E-1024; SparkFun Electronics) to detect and record real-time running velocity. The rotary encoder was attached to a running wheel and connected with a microcontroller (Arduino UNO R3; SparkFun Electronics). The running wheel (diameter, 14 cm; width, 8 cm) was made using a 3D printer (MakerBot Replicator

2; MakerBot). The microcontroller converted the digital inputs from the rotary encoder into analog signals reflecting running velocity, which was in turn recorded and analyzed with custom scripts written in MATLAB.

Calcium imaging and imaging data analysis

All imaging experiments were conducted on awake behaving mice under head-restraint in a dim, sound attenuated box. A one-photon imaging system modified from an Olympus BX51 microscope (Olympus Corporation, Shinjuku, Tokyo, Japan) with a 10 X objective (NA 0.3; Olympus, Cat. Number MPLFLN10x) was used to monitor GCaMP6 signals in behaving mice through the implanted GRIN lenses. The light source for imaging was a single-wavelength LED system (λ = 470 nm; https://www.coolled.com/) connected to the epifluorescence port of the Olympus BX51 microscope. The output power of the LED was set to 0.1-0.3 mW and was kept constant for the same subject across all imaging sessions. During imaging, the focus of the objective was adjusted such that the best dynamic fluorescence signals were at the focal plane. Visible landmarks, such as GCaMP6-expressing neurons and blood vessels, were used to help identify the same field of view (FOV) across different imaging sessions.

GCaMP6 fluorescence signals were captured with a monochrome CCD camera (pco.pixelfly, digital 14 bit CCD camera, image sensor ICX285AL) mounted onto the Olympus BX51. A custom Imaging Acquisition software written in LabVIEW (National Instruments) was used to interface the camera with a dedicated desktop computer and record the GCaMP6 signals at a frame rate of 10 frames/s. To synchronize imaging with behavioral events, Imaging Acquisition was triggered with a TTL (transistor-transistor logic) signal from the Bpod State Machine (Sanworks) used for behavioral control. During imaging, the timestamps of different events, including the trigger signals sent to Imaging Acquisition, CS onset, US onset and licking events, were all recorded with Bpod.

For imaging data processing and analysis, we first used Inscopix Data Processing software (v.1.2.0., Inscopix) to spatially down-sample all the raw images by a factor of 4 to reduce file size, and to correct the image stack for motion artifacts. The motion-corrected images were cropped to remove post-registration borders and margin areas. The pre-processed image stack was exported as a .tif file. Next, we used the extended constrained non-negative matrix factorization optimized for one-photon imaging (CNMF-E) (Pnev-matikakis et al., 2016; Xiao et al., 2020; Zhang et al., 2021; Zhang and Li, 2018; Zhou et al., 2018) to demix neural signals and get their denoised and deconvolved temporal activity, termed ΔF (Pnevmatikakis et al., 2016; Zhou et al., 2018). We used the output C_raw, which corresponds to a scaled version of ΔF, for further analysis.

To determine whether a neuron was significantly ($p < 0.05$) excited or suppressed by a stimulus, and thus can be classified as being "responsive" to the stimulus, we used the Wilcoxon signed-rank test to compare the mean ΔF values in a period immediately after stimulus onset (the durations of which are indicated in figure legends) with those in the 4 s baseline period in all the trials imaged. For further analyses, such as the population analyses, we used z-scores to represent the dynamic activities in each neuron. To obtain the temporal z-scores for a neuron, we first obtained the mean activity trace for the neuron by averaging the fluorescence signals (ΔF) at each time point across all trials, and then computed the z-scores as $(F(t) - F_{mean})/F_{SD}$, where $F(t)$ is the ΔF value at time t, F_{mean}, and F_{SD} are the mean and standard deviation, respectively, of the ΔF values over a 4 s baseline period.

To assess the temporal relationship between the onset of behavioral licking response and the onset of neuronal response, for each neuron, we calculated the z-scored neuronal activity at each time point and averaged the values across all trials; for the licking response, we calculated the licking rate at each time point (bin = 50 ms) and averaged the values across all trials. Next, we applied the change-point analysis (Gallistel et al., 2004; Paton et al., 2006) on these data to determine the time point at which the neuronal or behavioral response significantly changed (i.e., the change-point) following the presentation of CS. We repeated this for all neurons showing excitatory responses and calculated the difference between behavioral and neuronal change-points as the response delay for each neuron.

To analyze the trial-by-trial correlation between licking and neuronal responses, we first calculated the mean licking rate and the mean activity (z-scored) of each neuron during a specified time window (i.e., CS, US or baseline period) in each trial. We subsequently calculated the Pearson correlation coefficient between these two measures.

Evaluation of spatial clustering of neurons with specific functional properties

To test for spatial clustering of neurons with specific response properties at a relatively fine scale (tens of microns), we calculated pairwise distances between all neurons. We then examined the distribution of distances between neurons that were either similar or different in their response type(s) (i.e., excited by sucrose versus inhibited by sucrose).

Cell registration

To identify and track the same individual cells from images acquired in different imaging sessions, we performed cell registration as previously described (Sheintuch et al., 2017; Zhang et al., 2021; Zhang and Li, 2018). We used a probabilistic method which auto-matically registered cells across multiple imaging sessions and estimated the registration confidence for each registered cell. Briefly, we first used the CNMF-E analysis to generate the spatial footprints for all cells imaged in a reference session (e.g., sodium-depletion or early-learning session). We then repeated this process for the cells imaged in a target session (e.g., recovery from sodium-deple-tion or late-learning session). We used the footprints from the reference session as a reference map, and aligned with this map the footprints from the target session by correcting for translation and rotation differences between different sessions. We subsequently calculated the probability of a given pair of cells, each from one of the two imaging sessions, to be the same cell (P_{same}) based on their

spatial correlation and centroid distance. A pair of cells is considered to have the same identity if $P_{same} > 0.95$. The centroid distance between a pair of cells deemed to have the same identity is generally small ($\leq 6.5\ \mu m$).

Analysis of aIC^Fezf2 population dynamics in the activity space

To assess the relationship between aIC^Fezf2 population activity and different trial types in the go/no-go task, we used a previously described 'coding direction' analysis (Allen et al., 2019; Gao et al., 2018; Li et al., 2016; Xiao et al., 2020). For a population of n neurons, we found an $n \times 1$ vector in the n dimensional activity space that maximally separated the response vectors in two types of trials. We term this vector "coding direction (cd)." To obtain the cd of Hit and CR trials, for each neuron we first computed the average z-scored response in the two types of trials, r_{Hit} and r_{CR}, which are $n \times 1$ response vectors that describe the population response at each time point, t. We then computed the difference in the mean response vectors, $cd_t = r_{Hit} - r_{CR}$. We averaged the values of cd_t from CS onset to US onset to obtain a single cd. For a population of n neurons, this yielded an $n \times 1$ vector. The projection of population activity in Hit and CR trials along the cd was obtained as $cd^T r_{Hit}$ and $cd^T r_{CR}$, respectively.

Population vector analysis

To quantify learning-induced changes in the similarity between neuronal responses at population level, we performed population vector analysis as previously described (Rozeske et al., 2018; Zhang and Li, 2018). Briefly, we created a series of n-dimensional (n = number of neurons) activity vectors for the responses (z-scored) of individual neurons at each time point. Therefore, the ensemble neuronal response at a particular time point is represented by a vector with a dimension equal to the total number of neurons in that ensemble. We computed the Mahalanobis distance (MD) between the vectors as a measure of the similarity between ensemble neuronal representations. For example, the MD between the ensemble representations to CS and US in hit trials in the go/no-go task is defined as:

$$MD(CS_{Hit}, US_{Hit}) = \sqrt{(PV(CS_{Hit}) - PV(US_{Hit}))^T * S^{-1}(PV(CS_{Hit}) - PV(US_{Hit}))}$$

where $PV(CS_{Hit})$ and $PV(US_{Hit})$ are the individual and mean population vectors of responses to CS and US, respectively, in hit trials. S^{-1} is the inverse of the covariance matrix. The responses in a 3 s time window immediately after CS or US onset in the hit trials of the go/no-go task was used to generate the population vectors. The MD takes into account the differences in the means of the two sets of ensemble responses as well as their covariances.

For data visualization purpose, we used principal component analysis (PCA) for dimensionality reduction, and projected the population vectors onto a two-dimensional space.

Decoding analysis

We performed population decoding analysis using the linear support vector machine (SVM) in MATLAB (fitcsvm) to determine whether the types of trials could be predicted on the basis of the trial-by-trial population activities of aIC^Fezf2 or aIC^NTS neurons acquired in each session. We used the activities of all the simultaneously imaged neurons in each session to perform the population decoding analysis. To compare decoding accuracy between aIC^Fezf2 and aIC^NTS neurons, we pooled all the aIC^Fezf2 or aIC^NTS neurons and randomly sampled a certain number of neurons from each population to perform the population analysis (iteration: 100 times). First, we applied principal component analysis (PCA) on the matrix of z-scored trial-by-trial neuronal activities. We used the first two or three PCs to represent the population activity in each trial. We subsequently used a subset of the low dimensional trial-by-trial neuronal activity data as the training dataset to train a classifier with linear kernel function ('linear') for two-class decoding (e.g., classifying large-reward block and small-reward block). Finally, we validated the classifier by using the 'predict' function to classify the trial-by-trial neuronal activities in the test dataset. Activities from randomly selected 75% of trials of each type were used to train the classifier, and activities from the remaining 25% of trials of each type were used to test decoding accuracy. To generate the shuffled data, we randomly reassigned a trial type to each of the trial-by-trial neuronal activities. We then followed the same procedure as that used for classifying the actual data to decode the shuffled data. We repeated this classification process 1,000 times for both the actual test dataset and the shuffled data, and calculated the average accuracy as the decoding accuracy.

In vivo fiber photometry and data analysis

To record the activities of NTS^Recipient neurons or dopamine release in nucleus accumbens *in vivo* in behaving animals, we used a commercial fiber photometry system (Neurophotometrics Ltd., San Diego, CA, USA) to measure GCaMP6 or DA2m signals through an optical fiber implanted in the NTS or NAc core. A patch cord (fiber core diameter, 200 μm; Doric Lenses) was used to connect the photometry system with the implanted optical fiber. The intensity of the blue light ($\lambda = 470$ nm) for excitation was adjusted to a low level (20~50 μW) at the tip of the patch cord. Emitted fluorescence was bandpass filtered and focused onto the sensor of a CCD camera. Photometry signals and behavioral events were aligned based on an analog TTL signal generated by the Bpod. Mean values of signals from a region of interest were calculated and saved by using Bonsai software (Bonsai), and were exported to MATLAB for further analysis.

To correct for photobleaching of fluorescence signals (baseline drift), a bi-exponential curve was fit to the raw fluorescence trace and subtracted as follows:

$$F_{raw\_fit} = fit(Timestamp, F_{raw}, 'exp2')$$

$$F_{raw\_correction} = \frac{F_{raw} - F_{raw\_fit}}{F_{raw\_fit}}$$

After baseline drift correction, the fluorescence signals were z-scored relative to the mean and standard deviation of the signals in a time window -4 to 0 s relative to CS onset.
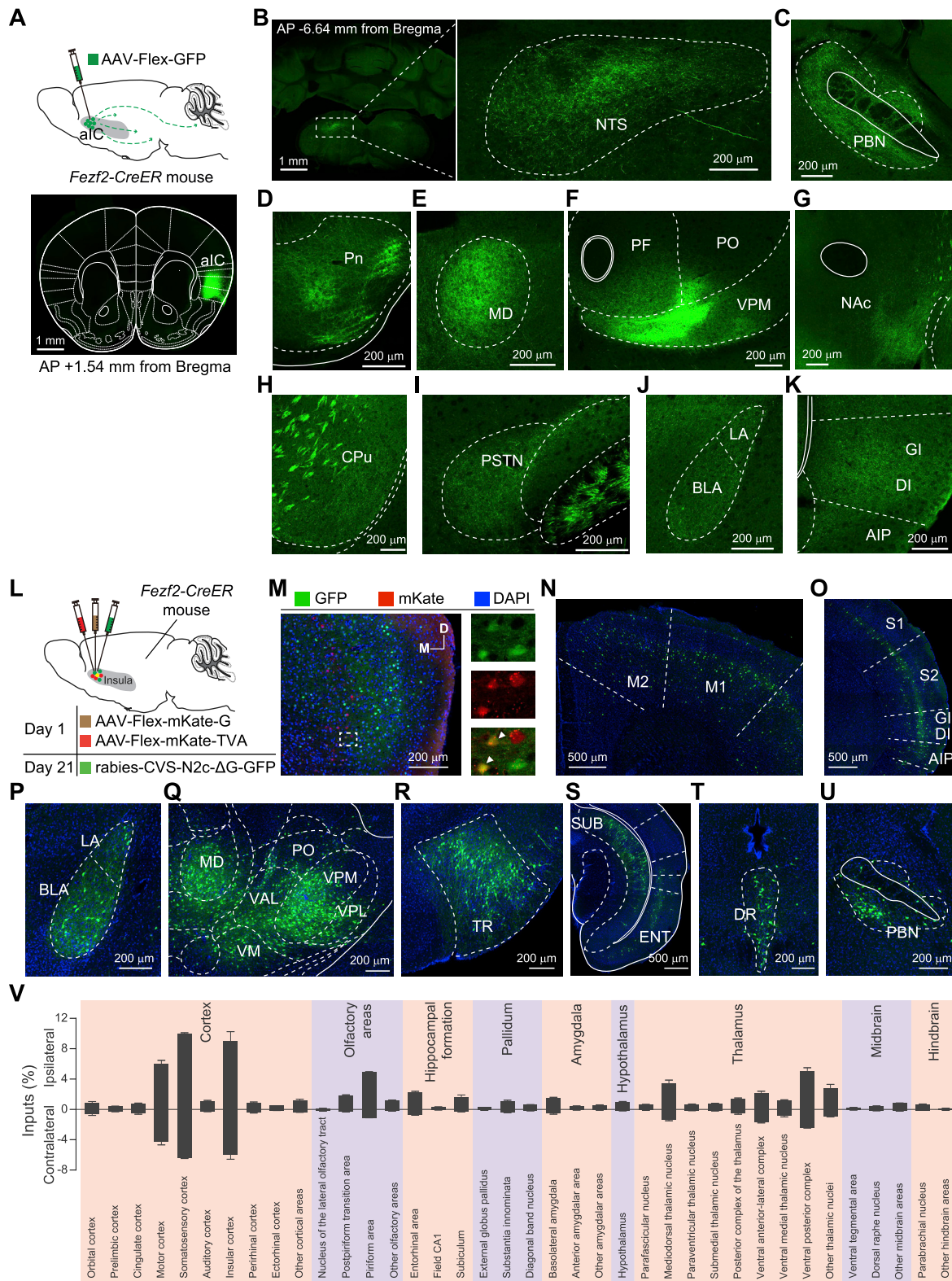
For the simultaneous optogenetic stimulation and photometry experiments, the mice received photostimulation in the NTS in the window between CS onset and US onset (3 s duration) in 33% of randomly selected trials, while we recorded DA2m fluorescence signals in NAc core using fiber photometry. The photostimulation parameters were 20-Hz pulse frequency, 10-ms pulse width, 5-mW power, 473-nm wavelength.

To identify pairs of laser-off and laser-on go trials with comparable lick rates, we first calculated the average lick rate from CS onset to US onset for each trial. We then searched all the laser-off trials for trials having the lick rates within 10% ± the rate of a laser-on trial. Of these, we then selected the laser-off trial that had a lick rate nearest to that of the laser-on trial. We compared the DA2m signals in such "matched" laser-off and laser-on trials. We used a lower power of laser for the stimulation to minimize the effect on licking, and thus increase the number of laser-on trials with lick rates comparable to those in laser-off trials.

QUANTIFICATION AND STATISTICAL ANALYSIS

Statistical analyses were performed using MATLAB or a commercial software (GraphPad Prism; GraphPad Software, CA). The statistical test used for each comparison is indicated when used. Analysis of variance (ANOVA) was used to check for main effects and interactions in experiments with repeated-measures and more than one factor. When main effects or interactions were significant, we did the planned comparisons according to experimental design (for example, comparing laser on and off conditions). All comparisons were two tailed. Threshold for significance was placed at $*p < 0.05$, $**p < 0.01$, $***p < 0.001$ and $****p < 0.0001$. The box-and-whisker plots indicate median, first and third quartiles, and min and max values. All data are shown as mean ± standard error of the mean (SEM) unless stated otherwise.

Supplemental figures

A AAV-Flex-GFP
Fezf2-CreER mouse
aIC
AP +1.54 mm from Bregma

B AP -6.64 mm from Bregma
NTS
1 mm
200 μm

C PBN
200 μm

D Pn
200 μm

E MD
200 μm

F PF PO VPM
200 μm

G NAc
200 μm

H CPu
200 μm

I PSTN
200 μm

J LA BLA
200 μm

K GI DI AIP
200 μm

L *Fezf2-CreER* mouse
Insula
Day 1 AAV-Flex-mKate-G
AAV-Flex-mKate-TVA
Day 21 rabies-CVS-N2c-ΔG-GFP

M GFP mKate DAPI
200 μm

N M2 M1
500 μm

O S1 S2 GI DI AIP
500 μm

P LA BLA
200 μm

Q MD PO VPM VAL VPL VM
200 μm

R TR
200 μm

S SUB ENT
500 μm

T DR
200 μm

U PBN
200 μm

V Inputs (%) Contralateral / Ipsilateral
Cortex | Olfactory areas | Hippocampal formation | Pallidum | Amygdala | Hypothalamus | Thalamus | Midbrain | Hindbrain

(legend on next page)

Figure S1. Output and input mapping of aIC^{Fezf2} neurons, related to Figure 1

(A-K) Mapping the projection targets of aIC^{Fezf2} neurons.

(A) Top, a schematic of the approach. Bottom, a representative confocal image showing the injection site and infection of aIC^{Fezf2} neurons with GFP.

(B) Representative confocal images showing axon terminals in the NTS, which originated from aIC^{Fezf2} neurons. On the right is a high magnification image of the boxed area on the left.

(C-K) Images showing aIC^{Fezf2} axon terminals in other target areas: parabrachial nucleus (C), pontine nuclei (D), mediodorsal thalamic nucleus (E), ventral posteromedial thalamic nucleus (F), nucleus accumbens (G), caudate putamen (H), parasubthalamic nucleus (I), lateral and basolateral amygdala (J), and posterior insular cortex (K). PF, parafascicular nucleus; PO, posterior complex of the thalamus; GI, granular insular cortex; DI, dysgranular insular cortex; AIP, agranular insular cortex, posterior part.

(L-V) Mapping the monosynaptic inputs onto aIC^{Fezf2} neurons.

(L) A schematic of the approach.

(M) Confocal images of a coronal brain section from a mouse prepared as in (L), showing the aIC^{Fezf2} neurons infected by the helper viruses (red) and the cells infected by the rabies virus (inputs, green). On the right are high magnification images of the boxed area on the left. Arrowheads indicate the starter cells (yellow).

(N-U) Representative images showing input neurons in the primary and secondary motor cortices (N), primary and secondary somatosensory cortices, and posterior insular cortex (O), lateral and basolateral amygdala (P), thalamus (Q), postpiriform transition area (R), subiculum and entorhinal area (S), dorsal raphe nucleus (T), and parabrachial nucleus (U). MD, mediodorsal thalamic nucleus; VAL, ventral anterior-lateral complex of the thalamus; VPM, ventral posteromedial thalamic nucleus; VPL, ventral posterolateral thalamic nucleus; VM, ventral medial thalamic nucleus; PO, posterior complex of the thalamus.

(V) Normalized distributions of rabies-labeled input neurons across different brain areas in each hemisphere (ipsilateral or contralateral to the injection site; n = 3 mice).
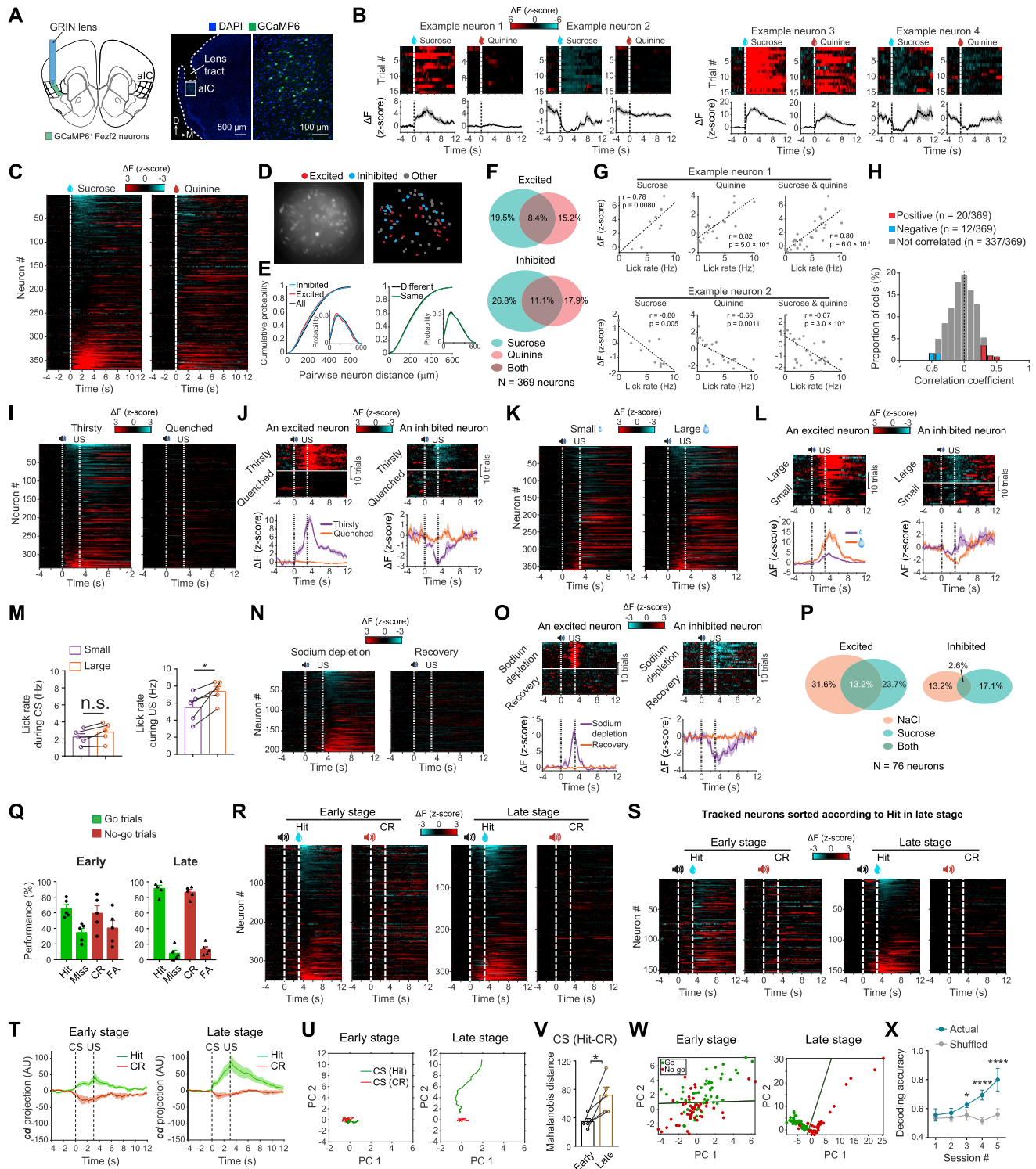
Data are presented as mean ± s.e.m.

Figure S2. Imaging aIC^Fezf2 neuron activity in behaving mice, related to Figures 1 and 2

(A-H) Imaging during the consumption of sucrose and quinine

(A) Left, a schematic of the approach. Middle, a representative confocal image showing GCaMP6f-expressing aIC^Fezf2 neurons and GRIN-lens placement over the aIC. Right, a high magnification image of the boxed area in the middle.

(B) Example aIC^Fezf2 neurons responding to sucrose and quinine. Trial-by-trial (top) and average (bottom) responses are shown for each neuron. Dashed lines indicate the onset of tastant delivery.

(C) Heatmaps of neuronal responses to sucrose (left) and quinine (right). Each row represents one neuron (N = 369 neurons from 5 mice). Rows are sorted by the response to sucrose and aligned to the onset of tastant delivery (dashed lines).

(D) Left, the field of view (FOV) of raw GCaMP6f fluorescence signals from aIC^{Fezf2} neurons in a representative mouse. Right, the spatial locations of individual extracted neurons in the FOV shown on the left. Different classes of neurons are color coded.

(E) Left, quantification of the pairwise distances of different classes of neurons in the FOV (excited versus inhibited, p = 0.26; excited versus all, **p = 0.0084; inhibited versus all, p = 0.062; Kolmogorov-Smirnov test). Right, quantification of the pairwise distances of neurons belonging to the same class ("same," i.e., the distances of excited-excited or inhibited-inhibited pairs; data were combined), and those belonging to different classes ("different," i.e., the distances of excited-inhibited pairs). These two distributions are not significantly different (p = 0.65; Kolmogorov-Smirnov test). Data are pooled from 5 mice.

(F) Percentage distributions of the neurons excited (top) or inhibited (bottom) by the tastants.

(G) Top, an example neuron (same as that shown in Figure 1F) showing a positive correlation between its responses and licking rates during US period. Graphs are plotted based on sucrose (left), quinine (middle) and pooled (right) trials. Bottom, same as top, except data were from a neuron showing a negative correlation. Each dot represents one trial.

(H) Distribution of all the neurons' Pearson's correlation coefficients calculated based on neuron activities and mouse licking rates during baseline period. Red, blue and gray bars represent neurons showing significant positive (p < 0.05), significant negative (p < 0.05) and nonsignificant (p > 0.05) correlations, respectively.

(I-P) Imaging during the reward-seeking task

(I) Heatmaps showing activity of all the aIC^{Fezf2} neurons in the reward-seeking task under thirsty (left) and quenched (right) conditions, with sucrose as the reward. Each row represents one neuron. Neurons are sorted based on responses in the anticipation period (0-3 s), with activities aligned to CS onset (first dashed line).

(J) Trial-by-trial (top) and average (bottom) response of two example neurons from those in (I), with one showing excitatory (left) and the other showing inhibitory (right) response to CS in thirsty (but not quenched) condition.

(K) Heatmaps showing activity of all the aIC^{Fezf2} neurons in the reward-seeking task under small-reward (left) and large-reward (right) conditions, with sucrose as the reward. Each row represents one neuron. Neurons are sorted based on responses in the anticipation period (0-3 s) under large-reward condition, with activities aligned to CS onset (first dashed line).

(L) Trial-by-trial (top) and average (bottom) response of two example neurons from those in (K), with one showing excitatory (left) and the other showing inhibitory (right) response to CS.

(M) Average licking rates during anticipation period (left, 0-3 s) ($t_{(4)}$ = 2.704, n.s., p = 0.054, paired t test) and US period (right, 3-5 s) ($t_{(4)}$ = 2.93, *p = 0.043, paired t test) in small-reward and large-reward conditions.

(N) Heatmaps showing activity of all the aIC^{Fezf2} neurons traceable in both sodium-depletion (left) and after recovery (right) conditions, with NaCl as the reward. Each row represents one neuron. Neurons are sorted based on responses in the US period (3-5 s) under sodium-depletion condition.

(O) Trial-by-trial (top) and average (bottom) response of two example neurons from those in (N), with one showing excitatory (left) and the other showing inhibitory (right) response to CS in sodium-depletion condition (but not after recovery).

(P) Percentage distributions of the neurons excited (left) or inhibited (right) by the consumption of NaCl in sodium-depletion condition, or by the consumption of sucrose solution in thirsty condition. A total of 76 neurons were traceable in both conditions.

(Q-X) Imaging during the go/no-go task

(Q) Performance of mice (n = 5) at the early (left) and late (right) training stages in the go/no-go task.

(R) Heatmaps showing the activities of all the neurons at the early (left) and late (right) training stages. At each stage, each row represents the activities of one neuron, and neurons are sorted based on their response during the US period (3-5 s) in hit trials.

(S) Heatmaps showing the activities of all the neurons traceable at both the early (left) and late (right) training stages. Each row represents the activities of one neuron across both training stages, and neurons are sorted based on their response during the US period (3-5 s) in hit trials at the late learning stage.

(T) aIC^{Fezf2} neuron population activity in hit and CR trials projected onto a coding direction (cd). Data were pooled from 5 mice at both training stages. AU, arbitrary unit.

(U) The trajectories of trial-averaged aIC^{Fezf2} population activity during CS period after dimensionality reduction with principal component analysis (PCA). Data were from a representative mouse at the early (left) and late (right) stages.

(V) Quantification of Mahalanobis distance between vectors representing CS responses in hit and CR trials ($t_{(4)}$ = 2.88, *p = 0.045, paired t test).

(W) An example of support vector machine (SVM) decoding using the principal components (PCs) of aIC^{Fezf2} population activity during CS period. The responses at the early (left) and late (right) training stages were used for the analysis.

(X) Learning improved the accuracy of aIC^{Fezf2} population CS responses in decoding go versus no-go trials ($F_{(4,20)}$ = 14.74, p < 0.0001; *p = 0.020, ****p < 0.0001; two-way ANOVA followed by Bonferroni's test). Actual, decoding analysis using the actual responses of neurons in go and no-go trials; shuffle, decoding analysis using the responses of neurons that were shuffled across trial types.

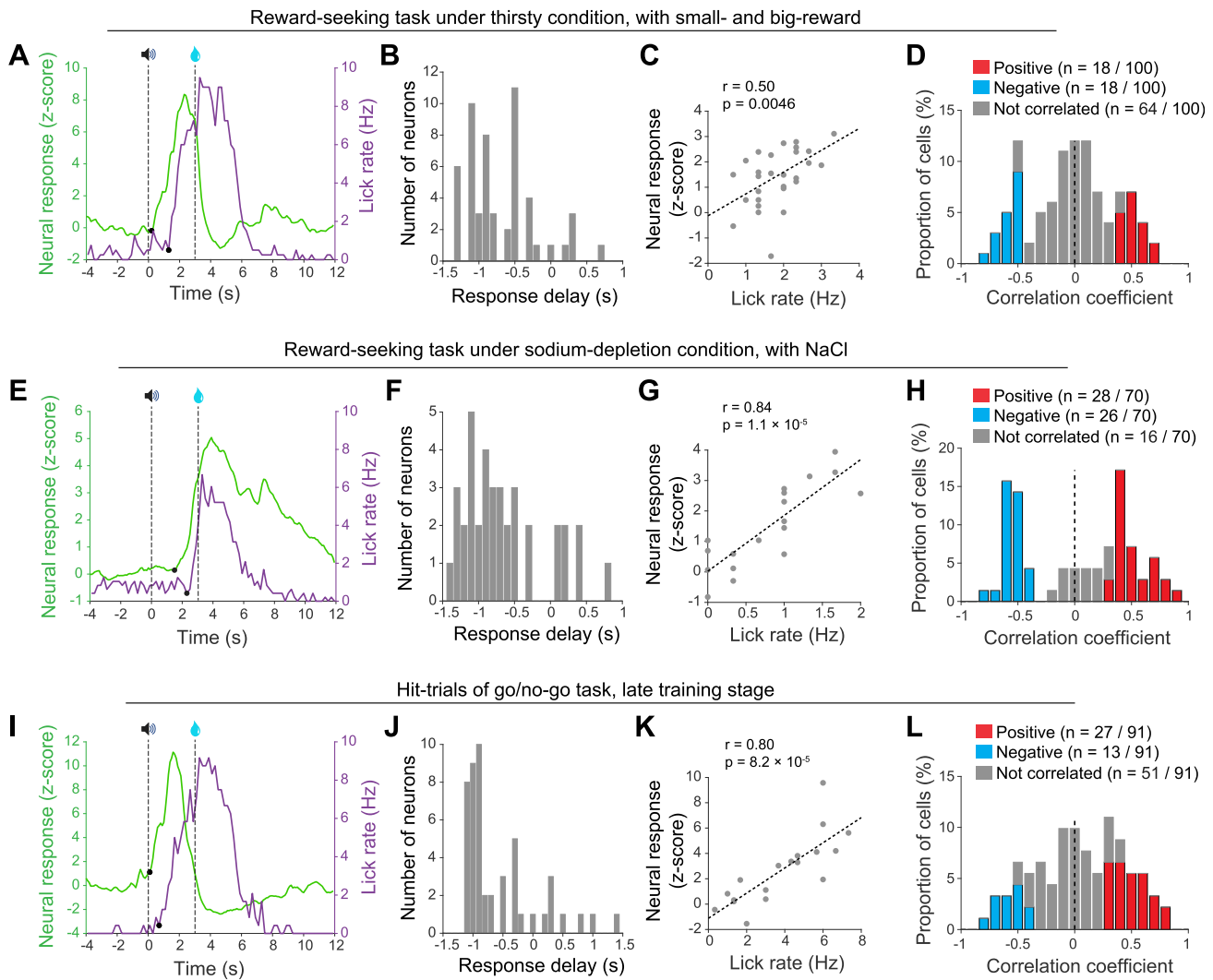Data are presented as mean ± s.e.m. Shaded areas around traces represent s.e.m.

Figure S3. The relationship between aIC^Fezf2 neuron activity and behavioral response, related to Figures 1 and 2

(A-D) Data acquired in the reward-seeking task under thirsty condition, with small- and large-reward as the US.

(A) The timing of CS-induced excitation in a representative aIC^Fezf2 neuron, and the timing of CS-induced increase in licking in the corresponding mouse determined by change-point analysis. Both neural activity (green) and licking behavior (purple) are aligned to CS onset. Black dots represent change points.

(B) Quantification of the difference between neural and behavioral change-points, for all the CS-excited neurons. Negative values indicate that neural response precedes behavioral response.

(C) An example neuron showing a positive correlation between its responses and licking rates during the anticipation (0-3 s) period. Each dot represents one trial.

(D) Distribution of all the CS-responsive neurons based on their Pearson's correlation coefficients calculated as in (C). Red, blue and gray bars represent neurons showing significant positive (p < 0.05), significant negative (p < 0.05) and nonsignificant (p > 0.05) correlations, respectively.

(E-H) Same as A-D, except that data are from the reward-seeking task under sodium-depletion condition, with NaCl as the US.

(I-L) Same as A-D, except that data are from hit trials in the late stage of the go/no-go task.
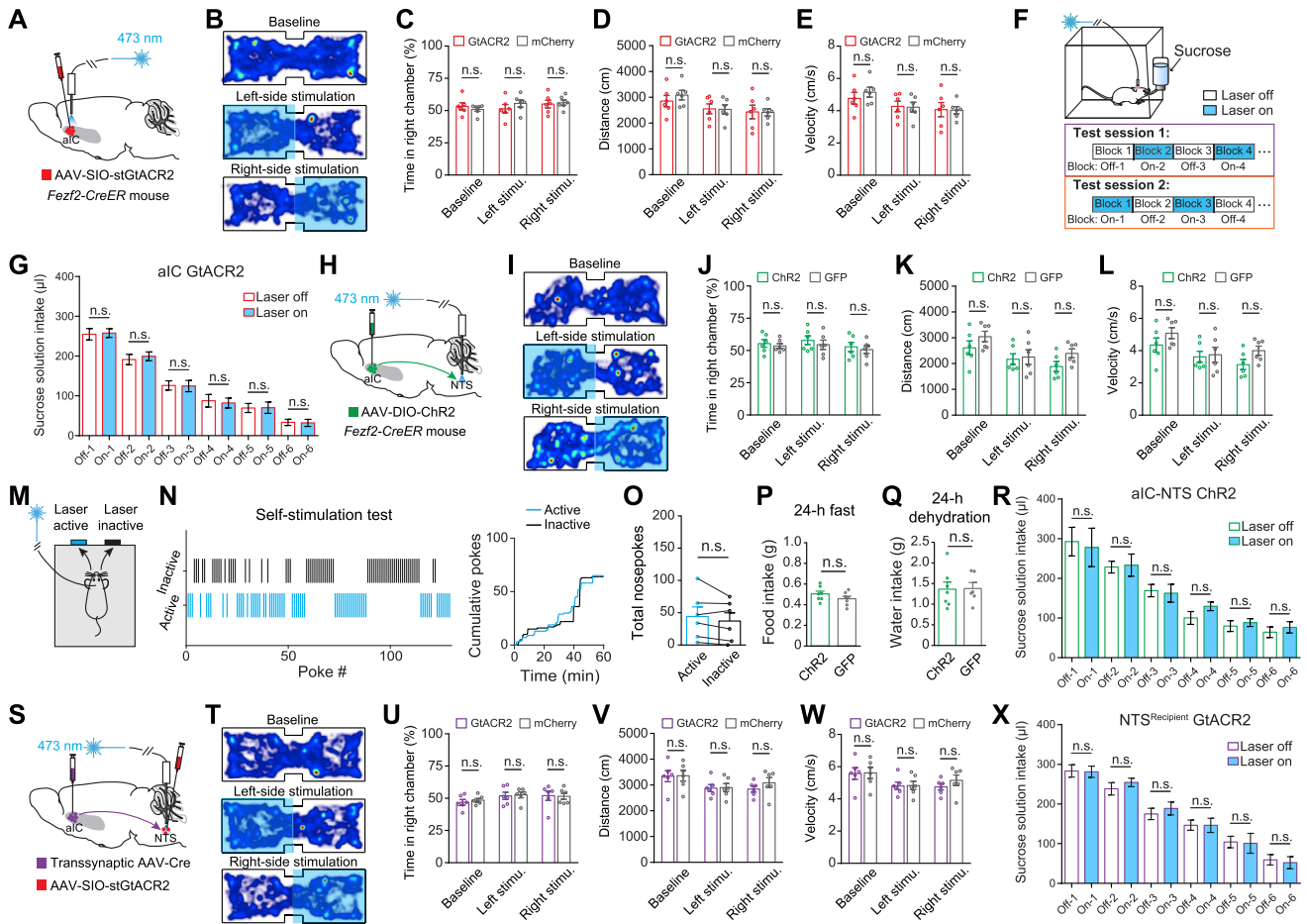
Figure S4. Manipulation of neuronal activity in aIC^Fezf2→NTS circuit does not affect movement, induce valence, drive reinforcement, or influence consumption, Related to Figures 2, 3, and 6

(A-G) Optogenetic inhibition of aIC^Fezf2 neurons

(A) A schematic of the approach for optogenetic inhibition of aIC^Fezf2 neurons.

(B) Heatmaps for the activity of a representative GtACR2 mouse at baseline (top), or receiving photo-inhibition once entering the left (middle) or right (bottom) side of the chamber.

(C-E) Quantification of behavior of the GtACR2 (n = 6) and mCherry (n = 6) mice, showing that inhibition of aIC^Fezf2 neurons does not induce place preference or aversion (C) ($F_{(2,30)} = 0.74$, $p = 0.49$), affect distance traveled (D) ($F_{(2,30)} = 0.27$, $p = 0.77$), or affect movement velocity (E) ($F_{(2,30)} = 0.27$, $p = 0.76$). Two-way ANOVA followed by Bonferroni's test.

(F) Schematics of the experimental setup (top) and design (bottom) for testing the effect of optogenetics on sucrose intake.

(G) Inhibition of aIC^Fezf2 neurons had no effect on sucrose intake (n = 7 mice, tested in 14 sessions; $F_{(5,78)} = 0.11$, $p = 0.98$; two-way ANOVA followed by Bonferroni's test.

(H-R) Optogenetic activation of aIC^Fezf2→NTS

(H) A schematic of the approach for optogenetic activation of aIC^Fezf2→NTS pathway.

(I) Heatmaps for the activity of a representative ChR2 mouse at baseline (top), or in a situation whereby entering the left (middle) or right (bottom) side of the chamber triggered photoactivation of aIC^Fezf2→NTS pathway.

(J-L) Quantification of behavior of the ChR2 (n = 6) and GFP (n = 6) mice, showing that aIC^Fezf2→NTS activation does not induce place preference or aversion (J) ($F_{(2,30)} = 0.033$, $p = 0.97$), affect distance traveled (K) ($F_{(2,30)} = 0.54$, $p = 0.59$), or affect movement velocity (L) ($F_{(2,30)} = 0.54$, $p = 0.59$). Two-way ANOVA followed by Bonferroni's test.

(M) A schematic of the self-stimulation test.

(N, O) Optogenetic activation of aIC^Fezf2→NTS does not support self-stimulation.

(N) Left, poking events at one port where poking triggered the photoactivation of aIC^Fezf2→NTS (active), and the other port where poking did not trigger the photostimulation (inactive) from an example session of a ChR2 mouse. Right, cumulative curves for the poking responses as shown in left.

(O) Quantification of the poking responses in the self-stimulation test for ChR2 mice (n = 6; $t_{(5)} = 1.5$, $p = 0.19$, paired t test).

(P) Quantification of the effect of photostimulation on food intake following 24-h food deprivation for the ChR2 (n = 7) and GFP (n = 7) mice ($t_{(12)} = 1.31$, $p = 0.22$, t test).

(Q) Quantification of the effect of photostimulation on water intake following 24-h water deprivation for the ChR2 (n = 7) and GFP (n = 6) mice ($t_{(11)} = 0.071$, $p = 0.94$, t test).

(R) aIC^{Fezf2}→NTS activation had no effect on sucrose intake (n = 6 mice, tested in 12 sessions; $F_{(5,66)}$ = 0.44, p = 0.82; two-way ANOVA followed by Bonferroni's test).

(S-X) Optogenetic inhibition of NTS^{Recipient} neurons

(S) A schematic of the approach for optogenetic inhibition of NTS^{Recipient} neurons.

(T) Heatmaps for the activity of a representative GtACR2 mouse at baseline (top), or in a situation whereby entering the left (middle) or right (bottom) side of the chamber triggered photo-inhibition of NTS^{Recipient} neurons.

(U-W) Quantification of behavior of the GtACR2 (n = 6) and mCherry (n = 6) mice, showing that inhibiting NTS^{Recipient} neurons does not induce place preference or aversion (U) ($F_{(2,30)}$ = 0.081, p = 0.92), affect distance traveled (V) ($F_{(2,30)}$ = 0.26, p = 0.77) or affect movement velocity (W) ($F_{(2,30)}$ = 0.26, p = 0.77). Two-way ANOVA followed by Bonferroni's test.

(X) Inhibition of NTS^{Recipient} neurons had no effect on sucrose intake (n = 6 mice, tested in 12 sessions; $F_{(5,66)}$ = 0.22, p = 0.95; Two-way ANOVA followed by Bonferroni's test).

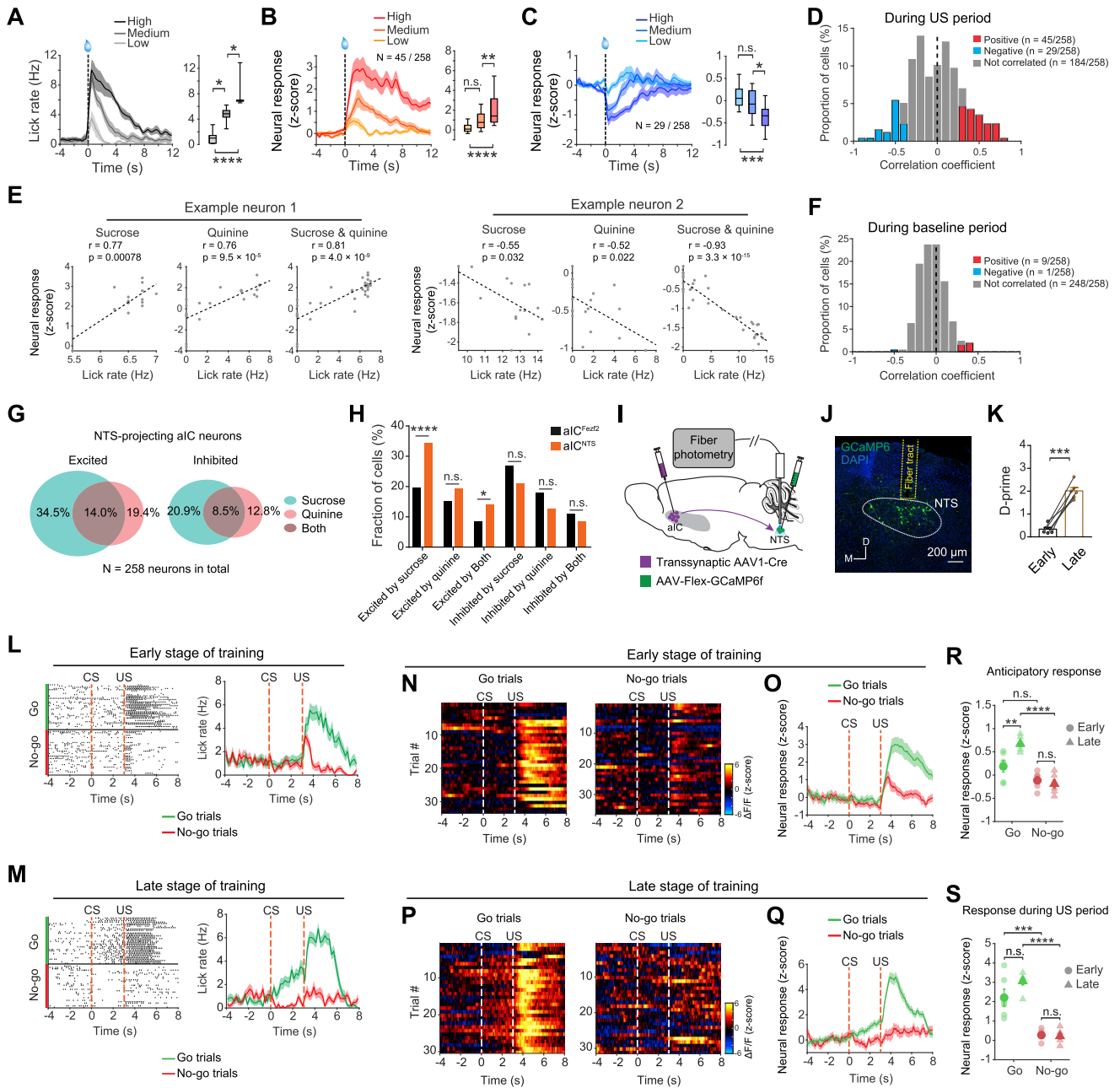Data are presented as mean ± s.e.m. n.s., non-significant (p > 0.05).

Figure S5. The *in vivo* activity of aIC^NTS neurons and NTS^Recipient neurons, related to Figure 5

(A–H) Imaging the *in vivo* activity of aIC^NTS neurons

(A) Left, average licking rates in different trial types (low, medium and high) classified based on the licking rates during the 4 s period after tastant delivery (dashed line). Right, quantification of average licking rates during the 4 s period following tastant delivery ($F_{(2,15)}$ = 21.03, p < 0.0001; *p = 0.011 (low versus medium), *p = 0.019 (medium versus high), ****p < 0.0001; one-way ANOVA followed by Tukey's test).

(B) Left, average responses of aIC^NTS neurons showing significant positive correlations in (D) in different trial types, which were classified as in (A). Right, quantification of average responses of the neurons during the 4 s period following tastant delivery ($F_{(2,132)}$ = 17.13, p < 0.0001; **p = 0.0016, ****p < 0.0001; n.s., nonsignificant; one-way ANOVA followed by Tukey's test).

(C) Same as (B), except that the neurons are those showing significant negative correlations in (D) ($F_{(2,84)}$ = 8.09, p = 0.0006; *p = 0.021, ***p = 0.0005; n.s., nonsignificant; one-way ANOVA followed by Tukey's test).

(D) Distribution of neurons based on the trial-by-trial Pearson's correlation coefficients between their average activities and the licking rates of the mouse during the 4 s period following tastant delivery. Red, blue and gray bars represent neurons showing significant positive (p < 0.05), significant negative (p < 0.05) and nonsignificant (p > 0.05) correlations, respectively.

(E) Neuron 1, an example neuron showing a positive correlation between its responses and licking rates during US period. Graphs are plotted based on sucrose (left), quinine (middle) and pooled (right) trials. Neuron 2, same as neuron 2, except data were from a neuron showing a negative correlation. Each dot represents one trial.

(F) Distribution of neurons according to the Pearson's correlation coefficients calculated based on neuron activities and mouse licking rates during baseline period. Red, blue and gray bars represent neurons showing significant positive ($p < 0.05$), significant negative ($p < 0.05$) and nonsignificant ($p > 0.05$) correlations, respectively.

(G) Percentage distributions of the aIC^{NTS} neurons excited (left) and inhibited (right) by sucrose or quinine, or by both tastants.

(H) Comparison of the fractions of aIC^{Fezf2} and aIC^{NTS} neurons showing responses to sucrose, quinine, or both tastants (excited by sucrose, ****$p < 0.0001$; excited by quinine, $p = 0.19$; excited by both, *$p = 0.035$; inhibited by sucrose, $p = 0.11$; inhibited by quinine, $p = 0.95$; inhibited by both, $p = 0.35$; n.s., nonsignificant; χ^2 test).

(I-S) Recording the activity of NTS^{Recipient} neurons during learning in the go/no-go task

(I) A schematic of the approach to target NTS^{Recipient} neurons for *in vivo* fiber photometry.

(J) A representative confocal image showing the expression of GCaMP6f in NTS^{Recipient} neurons and the placement of optical fiber for photometry.

(K) Quantification of D-prime at early and late stages ($t_{(5)} = 9.40$, ***$p = 0.0002$, paired t test).

(L) Licking events (left) and average licking rates (right) of a representative mouse at the early stage of training in the go/no-go task.

(M) Same as (L), except that data are from the same mouse at the late stage of training.

(N, O) Trial-by-trial heatmaps (N) and trial-averaged (O) GCaMP6 signals from NTS^{Recipient} neurons in a representative mouse at the early stage of training.

(P, Q) Same as (N, O), respectively, except that data are from the same mouse at the late stage of training. NTS^{Recipient} activity represents reward anticipation and evolves during learning.

(R, S) Quantification of the responses of NTS^{Recipient} neurons across training in all mice (n = 6) during anticipation period (0-3 s) (R) ($F_{(1,20)} = 9.89$, $p = 0.0051$; go-trials, early versus late, **$p = 0.005$; no-go trials, early versus late, n.s., $p = 0.93$; early, go versus no-go, n.s., $p = 0.12$; late, go versus no-go, ****$p < 0.0001$) and US period (3-5 s) (S) ($F_{(1,20)} = 3.16$, $p = 0.091$; go trials, early versus late, n.s., $p = 0.12$; no-go trials, early versus late, n.s., $p > 0.99$; early, go versus no-go, ***$p = 0.0002$; late, go versus no-go, ****$p < 0.0001$).Two-way ANOVA followed by Tukey's test.

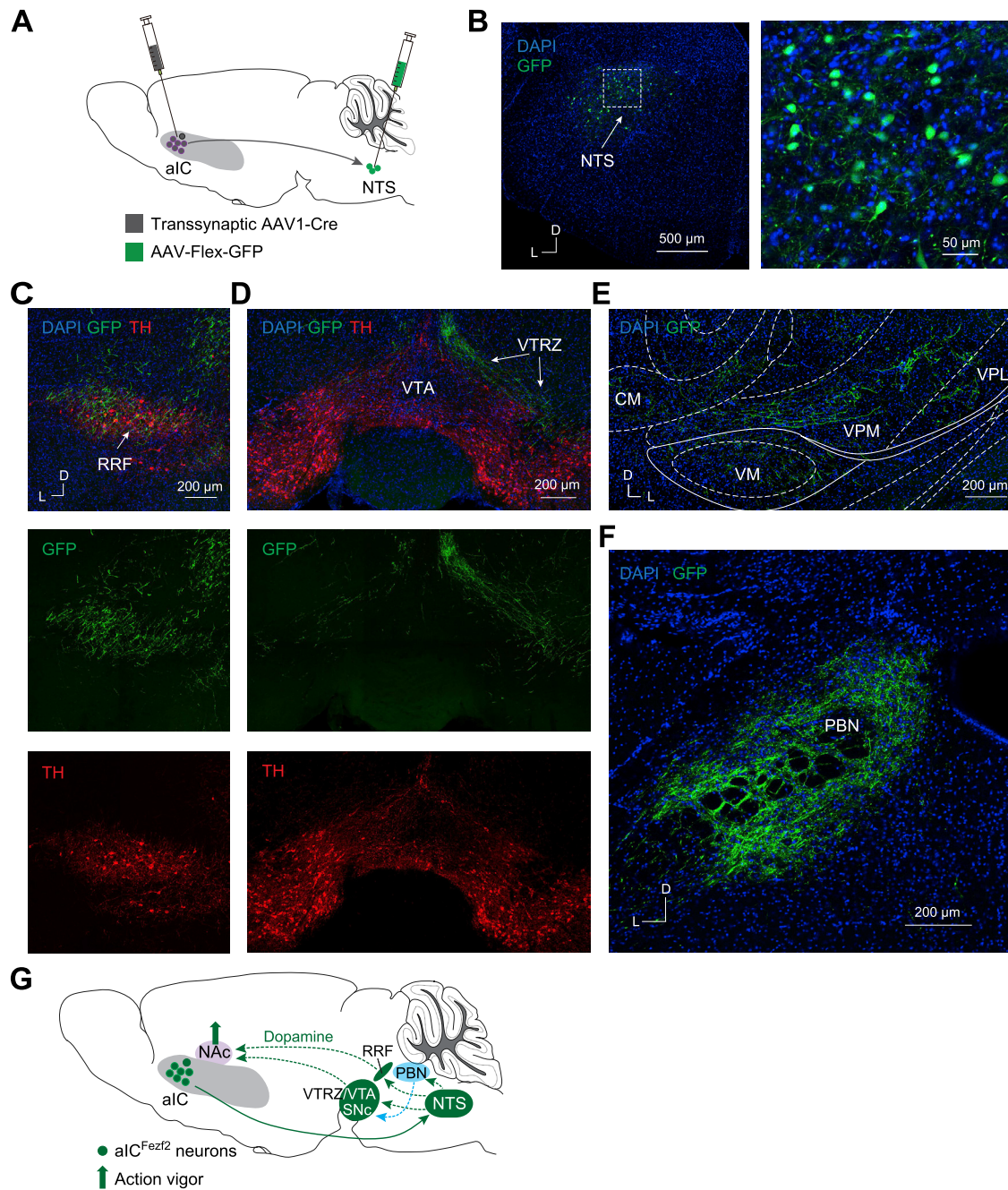Data are presented as mean ± s.e.m. Shaded areas around traces represent s.e.m.

Figure S6. Anterograde tracing of NTS^Recipient neurons, related to Figure 7

(A) A schematic of the approach to trace the projection targets of NTS^Recipient neurons.

(B) Representative confocal images showing GFP labeled NTS^Recipient neurons. On the right is a high-magnification image of the boxed area on the left.

(C, D) Representative confocal images showing GFP-labeled NTS^Recipient neuron axon terminals in the retrorubral field (RRF) (C) and visual tegmental relay zone (VTRZ) (D). Dopamine neurons were labeled by an antibody recognizing tyrosine hydroxylase (TH; red).

(E, F) Representative confocal images showing GFP-labeled NTS^Recipient neuron axons in the thalamus (E) and PBN (F). VPM, ventral posteromedial thalamic nucleus; VPL, ventral posterolateral thalamic nucleus; VM, ventral medial thalamic nucleus; CM, central medial thalamic nucleus.

(G) A model diagram showing components of the aIC-NTS circuit that participate in the regulation of action vigor. Dashed lines indicate the potential downstream pathways.